Thesis for a Ph.D. Degree

Trend analysis of new particle formation and subsequent growth: A regional and global perspective

지역 및 전구적 관점에서의 이차 입자 생성 및 후속 성장 경향 분석

August 2023

School of Earth and Environmental Sciences
Graduate School
Seoul National University

Do-Hyeon Park

Trend analysis of new particle formation and subsequent growth: A regional and global perspective

지역 및 전구적 관점에서의 이차 입자 생성 및 후속 성장 경향 분석

지도교수 김 상 우

이 논문을 이학박사 학위논문으로 제출함
2023년 5월

서울대학교 대학원
지구환경과학부
박 도 현

박도현의 이학박사 학위논문을 인준함
2023년 7월

위 원 장 박 록 진 (인)
부위원장 김 상 우 (인)
위 원 염 성 수 (인)
위 원 이 미 혜 (인)
위 원 윤 영 준 (인)

Trend analysis of new particle formation and subsequent growth: A regional and global perspective

By

Do-Hyeon Park

A Dissertation Submitted to the Faculty of the Graduate School of the Seoul National University in Partial Fulfillment of the Requirement for the Degree of Doctor of Philosophy

Degree Awarded:

August 2023

Advisory committee:

Professor	Rokjin J. Park, Chair
Professor	Sang-Woo Kim, Advisor
Professor	Seong Soo Yum
Professor	Meehye Lee
Doctor	Young-Jun Yoon

Abstract

Major secondary inorganic species and chemical processes associated with new particle formation (NPF) events in the free troposphere (FT) over the Korean Peninsula were characterized using aircraft observations conducted during Korea-United States Air Quality (KORUS-AQ) campaign (May–June 2016). During the FT NPF case (31 May, 2016) over the yellow sea, conversion of SO_2 to sulfate seemed to highly influence the NPF event. Sulfate-to-CO ratio had a positive correlation with both the temperature and relative humidity, implying that not only aqueous-phase pathways, but also gas-phase reactions might be attributed to sulfate formation. Particularly, FT NPF event on 31 May can be possibly connected to the favorable conditions for NPF occurrence in the FT, such as decreased aerosol surface area and increased solar radiation under the transport of SO_2 precursors from continent to shallow marine boundary layer. Additionally, an elaboration on the overall NPF characteristics during the KORUS-AQ campaign was conducted through the vertical profile of the number concentration of ultrafine particles with diameters between 3 nm and 10 nm (N_{CN3-10}). N_{CN3-10} during the entire KORUS-AQ period showed maximum (7606 ± 12003 cm^{-3}) at below 1 km altitude, suggesting that NPF events around the Korean Peninsula were frequent or intense in boundary layer (BL)

rather than FT.

Impacts of emission changes in atmospheric precursors on NPF occurrence can be complex as it is determined by the relationship between the concentration of precursor vapors and condensation/coagulation sink built by pre-existing large particles. The impact of the temporal variability in condensing vapors on the particle number size distribution (PNSD) and NPF over Asian continental outflow was evaluated based on the PNSD observation at three regional lowland background sites during the Coronavirus disease 2019 (COVID-19) lockdown (LD) period. The number concentrations of nucleation- (< 25 nm) and accumulation-mode (> 90 nm) particles significantly decreased in Baengryeong (BRY) during the LD period, showing ~34% and ~29% decreases, respectively. However, PNSD in Anmyeon (AMY) showed only a slight decrease in nucleation-/accumulation-mode particles under the impact of local emissions. Bongseong (BOS) experienced similar variation in PNSD to that in BRY, but the reduction was weaker (11% and 24% in the nucleation- and accumulation- modes, respectively) because of its relatively higher altitude.

The cyclostationary empirical orthogonal function (CSEOF) technique was applied to the measured PNSDs to distinguish NPF event days from non-NPF days based on the objective numerical values. Because all three cyclostationary loading vectors of mode 1 extracted

from observed PNSD data represented the typical diurnal evolution pattern during the regional NPF events (i.e. banana-shape), corresponding mode 1 principal component amplitude was used to classify NPF events. Although favorable meteorological conditions for NPF occurrence was built up during the COVID-19 LD period, NPF frequency decreased by 7%, 1%, and 7% in BRY, AMY, and BOS, respectively. The sulfuric acid (H_2SO_4) proxy during NPF occurrence time (8–12 local hours) suggested that decrease of sulfuric acid proxy played a determining factor for suppression of NPF occurrence in AMY and BOS; however, NPF occurrence in BRY was not associated with the H_2SO_4 proxy level. Considering the synergetic effect made by absence of nearby local sources as well as low altitude, BRY was more likely to be influenced by the reduction in organic species from the continental sources than other sites under the saturation of H_2SO_4 proxy inferred from the highest H_2SO_4 proxy relative to CS ([H_2SO_4 proxy]/[CS]; ~13.684±13.715 ppb W m^{-2} s) during the NPF occurrence time.

As an expansion of spatial and temporal scale of the PNSD and NPF analysis, global PNSD data measured in the stations joining in-Situ AeRosol GAW Network (SARGAN) were analyzed. Among them, measurement sites whose available continuous data were longer than 5 years (27 sites; 8 urban, 15 rural, and 4 remote sites) were selected to elaborate on the environmental characteristics in PNSD and NPF. NPF

frequency estimated based on CSEOF technique was the highest in urban regions, occurring around 43% of total observation days. The relatively low NPF frequencies were generally estimated at the observation environments whose anthropogenic influences are minimal. In the ambient air, the difference in the magnitude of precursor emissions according to the observation environment can be a more important factor than NPF occurrence in the competitive relationship between precursor emissions and condensation or coagulation sink built by pre-existing large particles. PNSD analysis was conducted based on the systematic division of particle diameters: particle number concentration of total- (10–500 nm; N_{tot}), nucleation- (10–25 nm; N_{nuc}), and accumulation (100–500 nm; N_{acc}) mode particles. N_{nuc} ratio [$N_{nuc}/(N_{nuc}+N_{acc})$] became generally high (60–70%) in the urban sites with the highest N_{tot}, suggesting that the frequency or intensity of NPF is important for explaining N_{tot}. The uni-modal peak located at the lowest diameter (~19 nm) also implied the impact of NPF events on PNSD in urban sites. Significant impact of the NPF occurrence on PNSD was also identified in the global trend. All the statistically significant NPF frequency trends were negative regardless of observation environment. Most of the negative NPF frequency trends resulted in the negative N_{nuc} trends in most of the stations. Furthermore, decadal decrease of NPF frequency was closely connected to the statistically significant negative

trend of N_{50} (particle number concentration with the diameter larger than 50 nm) in all of the observation environments. This suggests the statistically significant negative NPF frequency trend can be associated with the global decadal decrease cloud condensation nuclei (CCN) number under the assumption regarding CCN-sized aerosols (N_{50}) as potential CCN.

Key Words: New particle formation, Particle number size distribution, Cloud condensation nuclei, CSEOF technique, Secondary inorganic aerosols, COVID-19 lockdown

Student Number: 2015-22658

Table of Contents

List of Figures

List of Tables

Chapter 1. Introduction

1.1 Background and Motivation

Many regions in East Asia, like China or the Korean Peninsula, have suffered from extreme haze events brought on by elevated concentrations of $PM_{2.5}$ (particulate matter with diameters ≤ 2.5 μm) (Liu et al., 2019; Park et al., 2021a). Particularly, secondary inorganic species such as sulfate, nitrate, and ammonium made up a substantial part (about 47%) of $PM_{2.5}$ in Seoul during the Korea-United States Air Quality (KORUS-AQ) campaign (May–June 2016), suggesting that the formation of submicron particles can play a significant role in the occurrence of haze events (Wang et al., 2016; NIER and NASA, 2017; Chu et al., 2021). Considering organic aerosols together, the secondary production accounts for up to about 75%, showing larger contribution to the $PM_{2.5}$ concentration observed in the DC-8 aircraft observations (NIER and NASA, 2017).

The regional new particle formation (NPF) and subsequent growth can be variously characterized according to the regions in different environments, affecting differently to the regional particle number size distributions (PNSD). For example, NPF occurrence was most rare in the polar regions during most of the seasons, meanwhile formation rate (FR)

of 10–25 nm particles increased in the regions polluted by anthropogenic emissions (Nieminen et al., 2018). Furthermore, the corresponding global seasonality of PNSD and condensation nuclei (CN) were also reported (Laj et al., 2020; Rose et al., 2021). Laj et al. (2020) mentioned that CN was generally enhanced during the warmer season due to the growth of boundary layer (BL) and active formation of secondary aerosols, showing highest level in the urban areas including both continental and coastal sites. Rose et al. (2021) also revealed that the contribution of the number of accumulation-mode particles with the diameter larger than 100 nm (N_{100}) to total CN numbers (N_{tot}) was lowest (< 75%) in the urban regions by the systematic presence of small particles from traffics, being increased in the winter under the emission of residential heating. Meanwhile, the contribution of N_{100} in the mountain areas was highest in the summer owing to the transport of larger particles related to BL dynamics, but lowest in the winter under the frequent occurrence of clouds, inducing the degradation of the sampling efficiency of larger particles (Rose et al., 2021). These works show the large difference in the PNSD and NPF according to the various environments, emphasizing the necessity for the global study for the variability of aerosol physical parameters.

The importance of NPF can be highlighted when the newly-formed particles successfully grow to the cloud condensation nuclei (CCN)-sized

aerosols (Kerminen et al., 2018). The regional NPF typically shows the enhancement of nucleation-mode particles and distinct subsequent growth, showing so-called 'banana-shape' on the plot of the PNSD with time. For that reason, the regional NPF showing significant growth pattern can be a significant contributor for CCN-sized aerosols. For example, the NPF taking place in 2014 at Vienna (urban background) contributed to the CCN concentration about 58% (de España et al., 2017). Also, Kerminen et al. (2012) documented that nucleation events enhanced the median maximum CCN concentrations at sites in various environments by hundreds of percent. Considering the reported importance of NPF in the aspect of the supplier of CCN, the global change of NPF with subsequent growth can be closely related to the change of CCN-sized aerosols, being involved with the aerosol indirect effect associated with the cloud formation and precipitation worldwide.

1.2 Scientific Questions

The above background leads to several central scientific questions to be studied. Specific scientific questions of this study consist of the three subjects as follows:

(1) What is the characteristics of particle number size distribution (PNSD) and new particle formation (NPF) over Asian continental outflow?

The regional NPF can take place not only in the BL but also free troposphere (FT). FT is characterized by the reduced influence of the primary emissions from the surface and favorable conditions (e.g. reduced surface area and increased sunlight) of NPF. Furthermore, particles formed in the FT can be entrained to the BL, thereby influencing on the air quality of the BL (Kerminen et al., 2018; Takegawa et al., 2020). However, despite the importance of NPF in the FT, few observations in the FT actually exist since they can only be conducted through limited methods, such as mountain-top observations (Bianchi et al., 2016; Shen et al., 2016; Lv et al., 2018). Although NPF events captured by ground-based observation in the mountain-top site can be related to the FT (Rose et al., 2017), they also can be often associated with the airmass originated from the BL following the daytime valley wind (Miao et al., 2015). The characteristics of FT NPF can be similar to the that of BL NPF under the daytime valley breeze, but relatively small amount of condensable vapors can result in the active FT NPF under above-mentioned favorable conditions compared to BL (Takegawa et al., 2020).

Despite the favorable conditions for NPF in the FT, anthropogenic condensing vapors originated from anthropogenic sources are primarily emitted in the BL. However, the Coronavirus disease 2019 (COVID-19) pandemic forced many countries to regulate anthropogenic activities in diverse fields, such as industrial processes and on-road mobile sources

(Shrestha et al., 2020; Venter et al., 2020). China executed intensive lockdown (LD) measures against the spread of COVID-19 in 95 cities starting in late January 2020 (He et al., 2020). During the Chinese COVID-19 LD period, the concentration of ambient air pollutants showed significant national variation compared to previous years. For example, overall reductions in principal anthropogenic air pollutants, such as $PM_{2.5}$, NO_2, CO, and SO_2, were observed at many monitoring stations operated by the China National Environmental Monitoring Center (Shi et al., 2020). However, even with the reduced emission of major gaseous air pollutants, unexpected haze events occurred owing to the efficient secondary formation of aerosols. Actually, Chang et al. (2020) analyzed the severe haze events induced by nitrogen chemistry and long-range transport during the COVID-19 LD period. Therefore, possible impacts of variability in gaseous precursors on PNSD and NPF needs to be evaluated because NPF properties can be more complexly affected by emission curtailment during the lockdown according to changes in atmospheric chemistry or regional-scale meteorology (Kim et al., 2016).

(2) How have the observed global PNSD and NPF been changed over past decades?

Under the significance of the aerosol physical parameter (e.g. particle number concentration) in terms of the air pollution and climate,

many aforementioned previous studies (Nieminen et al., 2018; Laj et al., 2020; Rose et al., 2021) discussed the seasonal and spatial variability of global NPF, CN, PNSD, respectively. Furthermore, multidecadal trends of aerosol optical (scattering, absorption, Ångstrom exponent) properties were reported in detail for the *in-situ* observation around the globe (Collaud Coen et al., 2020). Under the consistent air quality regulations associated with major atmospheric pollutants such as SO_2 (Kerminen et al., 2018; Aas et al., 2020), the connection between the change of the concentration of condensable vapors and NPF intensity (FR) are relatively well revealed (Yao et al., 2018) compared to the NPF frequency. However, a gradual interest has been concentrated on the connection between SO_2 concentration and NPF occurrence under the inconclusive observational evidences published by many previous works (Kerminen et al., 2018). Several literatures reported higher SO_2 concentration during NPF days (e.g. Zhao et al., 2015) because of the promotion of NPF occurrence via the formation of gas-phase sulfuric acid, while some papers documented that SO_2 concentration was lower during non-NPF days under higher condensation sink (CS) resulting in uptake of low-volatile organic compounds and molecular clusters (e.g. Dai et al., 2017). However, despite the global analysis associated with the seasonal and spatial variability of CN, PNSD, and NPF, the global change of these parameters over past decades was not reported until now, leaving a

question about their impact on decadal change of climate variables such as CCN. Under the absence of the global observations of CCN via CCN counter, the impacts of NPF on the global CCN concentrations were primarily studied using aerosol microphysics model (e.g. GLOMAP; Spracklen et al., 2008; Merikanto et al., 2009). Model-based estimation of contribution of nucleation to CCN budget implied that NPF can be a significant source of atmospheric CCN, accounting for about 45% of low-level cloud CCN (Merikanto et al., 2009). Although the CCN measurements have been conducted in several sites for many years, the number of CCN observations is not sufficient for understanding the relationship between the global change of NPF and CCN concentrations. Therefore, the observation-based investigation for the global link between the NPF and CCN based on the reasonable assumption would have implication in terms of relationship between NPF and CCN number concentration.

1.3 Objectives of this study

To answer these scientific questions, the overall goal of this study is to investigate the global trend of PNSD and NPF in the various environments. The results will aid in our understanding of decadal change of PNSD and NPF worldwide.

The specific objectives of this study are as follows:

(1) to investigate regional characteristics of PNSD & NPF over Asian continental outflow

The spatial characteristics of NPF over Asian continental outflow is understood based on the DC-8 aircraft observation of FT NPF with FT origin. Possible processes associated with FT NPF over East Asia are proposed via synergetic use of chemical transport model, aircraft observation, and ground-based observation of remote sensing. Furthermore, vertical distribution of ultrafine particles mainly formed by NPF events is identified through the comprehensive observation based on the all available flights during the KORUS-AQ campaign.

To evaluate the pandemic lockdown impact on the PNSD as well as NPF frequency over Asian continental outflow, *in-situ* PNSD observation at three Korean background sites during LD period in 2020 is analyzed. Using the cyclostationary empirical orthogonal function (CSEOF) technique, NPF frequency during the LD period is estimated in three sites. Possible cause of the change in NPF frequency is inferred based on the observations of major atmospheric precursors over East Asia.

(2) to conduct trend analysis of PNSD and NPF on the global scale

Before trend analysis, environmental characteristics is elaborated

based on multi-year PNSD observation from in-Situ AeRosol Global Atmosphere watch Network (SARGAN). To reveal the impact of the global NPF occurrence on PNSD, the global trends of PNSD and NPF frequency are investigated. Implications of the decadal changes in NPF occurrences are explored by examining the relationship between the global NPF change and CCN using a simple approach regarding CCN-sized aerosols as potential CCN.

Chapter 2. Measurements and analysis

Various observation instruments were used for the investigation of NPF case. The measured parameters and uncertainties of the instruments are given in **Table 2.1**. Among them, condensation particle counter (CPC) and scanning mobility particle sizer (SMPS) would be further described because they directly observe aerosol physical properties (e.g. particle number concentration), which is the main target variables of the entire study.

2.1 Condensation particle counter (CPC)

The number concentrations of aerosols with the diameters greater than 3 nm and 10 nm were observed using condensation particle counter (CPC)-3776 and 3010, respectively (Park et al., 2020). CPC measurement was conducted based on the aircraft platform for the case study. Firstly, the particles are dressed up until the measurable sizes. After the light is projected to the grown particles, and scattered-light pulses are detected and converted to the number densities. In this study, the particle numbers with the diameters between 3 nm and 10 nm ($N_{CN3\text{-}10}$) were derived by subtracting the number of particles larger than 10 nm from

that larger than 3 nm.

2.2 Mobility particle size spectrometer (MPSS)

MPSS, which is frequently represented as Scanning Mobility Particle Sizer (SMPS) or Differential Mobility Particle Sizer (DMPS) in many previous studies (Kim et al., 2021; Park et al., 2023), derives PNSD by counting particles classified based on their mobility. For the general description based on SMPS, the particles larger than the upper limit of the observations are generally filtered out by being collided to the cyclone installed in front part of the SMPS inlet. A population of particles is neutralized and endowed electric charges by radioactive chemical species such as Kr-85. The population of aerosols are separated in the differential mobility size analyzer (DMA) rod by their electrical mobility based on the relationship between aerosols size and the strength of electric field. Separated aerosols grow up to measurable sizes by the condensation of injected butanol and are counted by condensation particle counter (CPC) part in MPSS. For derivation of global PNSD, diverse mobility particle size spectrometer (MPSS) measurement with lower/upper size limit was used for the selected sites in the various observation environment. More detailed description associated with MPSSs is represented by Wiedensohler et al. (2012).

2.3 Cloud condensation nuclei (CCN) counter

CCN number concentration measurement has been conducted at five stations (Hyytiälä, Vavihill, Jungfraujoch, Zeppelin, Cape Grim) based on EBAS webpage (https://ebas-data.nilu.no/). Among them, all available CCN measurements in Hyytiälä (HYY; 2013–2020) and Vavihill (VAV; 2008–2016) were used to validate the assumption regarding CCN-sized aerosols as potential CCN, because only they are measuring PNSD as well as CCN number concentration. CCN number concentration was estimated at different supersaturation ratio (0.1%, 0.2%, 0.3%, 0.5%, 1.0% for Hyytiälä, and 0.1%, 0.2%, 0.4%, 0.7%, 1.0% for Vavihill) using CCN counter (DMT CCN-100). For different supersaturation ratio, if solute diameter is sufficiently large (> CCN-size), the solute grows to very large diameter because thermodynamic equilibrium cannot be satisfied according to Köhler theory. Supersaturated solutes are then counted by optical particle counter in CCN counter.

2.4 Cyclostationary empirical orthogonal function (CSEOF)

The cyclostationary empirical orthogonal function (CSEOF) technique was applied to the PNSD data observed at the three background stations. The CSEOF technique is an extended version of empirical orthogonal function analysis (Kim et al., 1996). In the CSEOF

technique, the PNSD hourly data (T) are decomposed into different modes of CSEOF loading vectors (CSLVs) multiplied with principal component (PC) time series as follows (Kim et al., 2013):

$$T(r,t) = \Sigma_n CSLV_n(r,t)PC_n(t)$$

where n is the number of CSEOF modes. In this study, both PNSD and CSLVs are the function of the size bins (r) and time (t). Also, the CSLVs are periodic in the nested period (d), $CSLV_n(r,t) = CSLV_n(r,t + d)$. Because NPF typically occurs during the daytime for a period of approximately one day, the nested period of the CSEOF analysis was set to 24 h. Accordingly, CSLVs display the temporal variation in daily PNSD, and PC time series denotes the amplitude of the pattern displayed by CSLVs (Kim et al., 2021; Park et al., 2021b).

Table 2.1. Descriptions for the instruments and measured parameters in the case study.

Instrument	Parameter	Uncertainty	Reference
Condensation particle counter (CPC)	Aerosol number concentration with diameters greater than 3 nm and 10 nm [cm^{-3}]	10%	Park et al. (2020)
Scanning mobility particle sizer (SMPS)	Particle size distribution [cm^{-3}]	20%	Jeong and Evans (2009) Kim et al. (2013) Kim et al. (2016)
Aerosol mass spectrometer (AMS)	Sulfate concentration (diameter < 1 μm) [$\mu g\ m^{-3}$]	Variable	DeCarlo et al. (2006)
Chemical ionization mass spectrometer (CIMS)	Sulfur dioxide (SO_2) mixing ratio [pptv]	30%	Huey et al. (2004) Slusher et al. (2004) Crounse et al. (2006)

Chapter 3. Characteristics of PNSD and NPF over Asian continental outflow

3.1 Spatial characterization of the NPF and PNSD over Korea

By taking advantage of aircraft observation, NPF cases of the FT origin during the KORUS-AQ campaign were investigated to contrast the major secondary inorganic species and possible processes. Although condensable organic vapors can play a significant role in NPF over Korean Peninsula (Choi et al., 2017; Kim et al., 2018), this study focused on the inorganic compounds because the composition of secondary inorganic aerosols was generally larger than that of organic aerosols during the KORUS-AQ campaign (Jordan et al., 2020). Based on the vertical profile of $N_{CN3\text{-}10}$ measurement via aircraft platform, meaningful FT altitude in terms of NPF was determined to be from 2 to 4 km, because $N_{CN3\text{-}10}$ dramatically decreased after 4 km altitude (**Fig. 3.5a**).

The 31 May case was expected to be influenced by pollutants from upwind regions (e.g., China) during the KORUS-AQ campaign (Peterson et al., 2019). To capture the impact of Chinese emissions from the observations, the DC-8 aircraft flew over the Yellow Sea (YS). The flight routes of the DC-8 during 31 May and the corresponding $N_{CN3\text{-}10}$ values are presented in **Figure 3.1a**. During 31 May, substantial $N_{CN3\text{-}10}$ (~2,000

cm^{-3}) was observed in the FT over the YS, and it even exceeded 5,000 cm^{-3} in the west of the SMA. In the time series of N_{CN3-10} during 31 May (**Fig. 3.1c**), N_{CN3-10} showed peaks at around 30,000–40,000 cm^{-3} during the flight in the FT, reflecting the occurrence of NPF event. About 0.006 km^{-1} sr^{-1} of backscatter coefficient was measured in the 2–3 km range under the influence of submicron particles formed in the FT (not shown). Based on these observations, 31 May was designated as the FT NPF case.

Figure 3.2 displays the time series of the secondary inorganic aerosols and their precursors during the FT NPF case. Generally, the SO_2-to-sulfate conversion seemed to highly influence the particle formation events in the FT because the sulfate concentration was changed along with the SO_2 mixing ratio. On the other hand, the NO_2 mixing ratio and nitrate concentration were nearly zero, suggesting that oxidation of NO_2 had little correlation with the NPF event on 31 May.

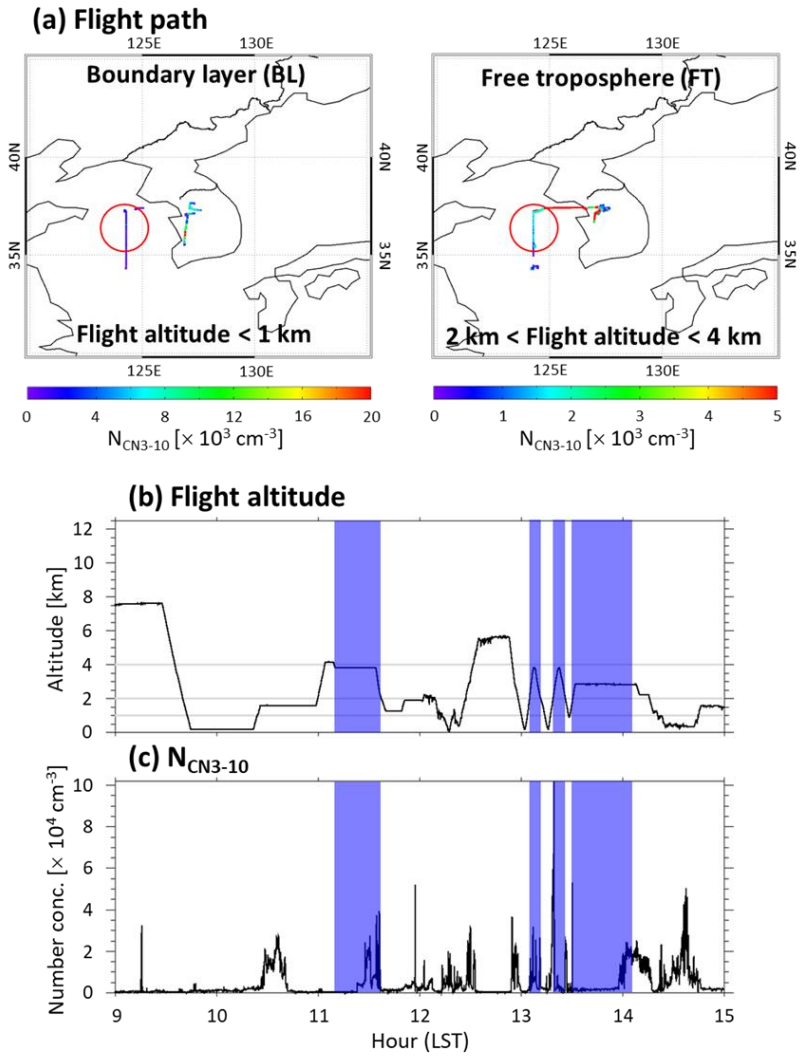

Figure 3.1. FT NPF case (31 May, 2016): (a) The flight path in the BL and FT. $N_{CN3\text{-}10}$ corresponding to the flight path is represented as color scale. (b) The time series of flight altitude. The light grey line is located at the 1 km, 2 km, 4 km altitudes. (c) The time series of $N_{CN3\text{-}10}$. The period of FT (2 km–4 km) flight over the YS is shaded as azure color.

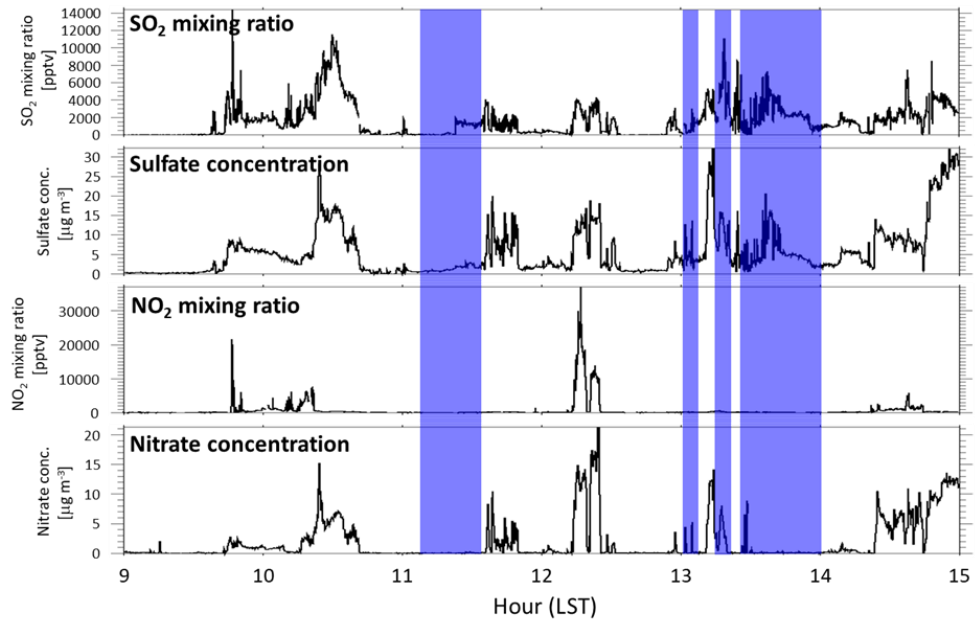

Figure 3.2. The time series of SO_2 mixing ratio, sulfate concentration, NO_2 mixing ratio, and nitrate concentration during the FT NPF case (31 May, 2016). The period of FT (2 km–4 km) flight over the YS is shaded as azure color.

Gas-phase reaction rates can positively be correlated with the temperature according to the Arrhenius equation (De Persis et al., 2004; Seinfeld and Pandis, 2016), while the aqueous-phase processes are known to occur more actively under humid environmental condition (Wu et al., 2019; Seinfeld and Pandis, 2016). Based on the theories, formation mechanisms of major secondary inorganic species during the case were investigated. Because the baseline level of the SO_2 mixing ratio is typically low in the FT compared to BL, a high SOR (sulfur oxidation ratio; $nSO_4^{2-}/(nSO_4^{2-}+nSO_2)$; Ji et al., 2018; Tian et al., 2019) would be derived even if

only a small amount of SO_2 was converted to sulfate or an abrupt variation in the SO_2 mixing ratio was induced by transport, degrading the meaning of SOR as an indirect indicator of the sulfate formation. For the FT NPF case, the sulfate-to-CO ratio was used instead of SOR because CO which has a relatively long lifetime is appropriate for tracing the change in sulfate (Ding et al., 2015). The sulfate-to-CO ratio had a positive correlation with both the temperature and relative humidity (RH), indicating that aqueous-phase pathways as well as gas-phase reactions might be attributed to the sulfate formation in the FT (**Fig. 3.3**). Many studies reported that aqueous-phase oxidation of SO_2 associated with the uptake processes on the surface of preexisting particles is the main pathway of sulfate formation, although the gas-phase reactions of SO_2 are significant as well (Khoder, 2002; Tsona et al., 2018; Liu et al., 2020); these findings are consistent with the results herein.

Due to the lack of continuous observation of atmospheric pollutants at high altitudes, the direct derivation of the general properties of NPF events in the FT during the entire KORUS-AQ campaign was limited. Rather than generalizing, investigation of the possible cause of the FT NPF case was conducted by simulating the behavior of SO_2 at 700 hPa using a chemical transport model (GEOS-Chem; **Fig. 3.4**). The migration of SO_2 and sulfate was simulated at the 700-hPa pressure level. The

mixing ratio of the transported SO_2 over the YS was expected to be maximum around 12:00 LST on 31 May, implying that the FT over the YS during 31 May could be suitable for the active sulfate formation. When the continental precursors are directly transported from deep continental boundary layer to relatively shallow marine boundary layer, the formation of particles could be facilitated in the FT under favorable conditions such as the lack of the preexisting particles and increase in the sunlight (Park et al., 2021a; Takegawa et al., 2020). The submicron particles produced by this mechanism can spread to FT or be entrained to the BL, thereby also having an influence on the air quality at the surface (Kerminen et al., 2018; Takegawa et al., 2020). This observation-based capture of FT NPF resulting from continental condensable vapors above shallow marine boundary layer was consistent to the formation of new particles in the FT over open seas derived from the Hydrological cycle in Mediterranean Experiment (HYMEX) project (Rose et al., 2015).

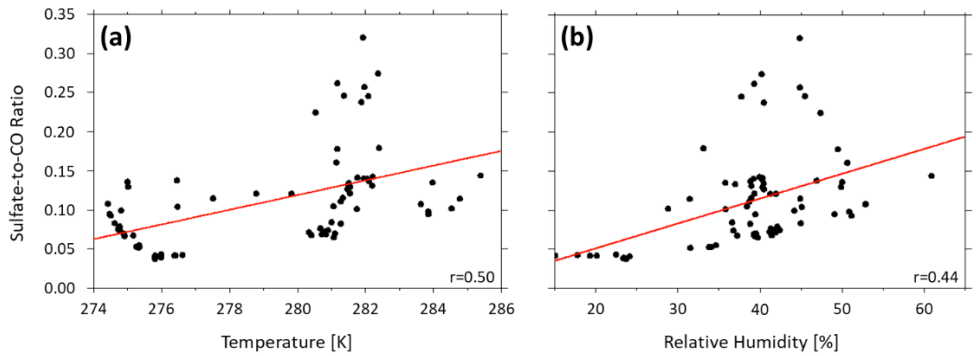

Figure 3.3. The scatter plot for sulfate-to-CO ratio versus (a) temperature and (b) relative humidity for DC-8 flight in FT over the YS during the FT NPF case (31 May, 2016). The linear regression lines are represented as red solid lines.

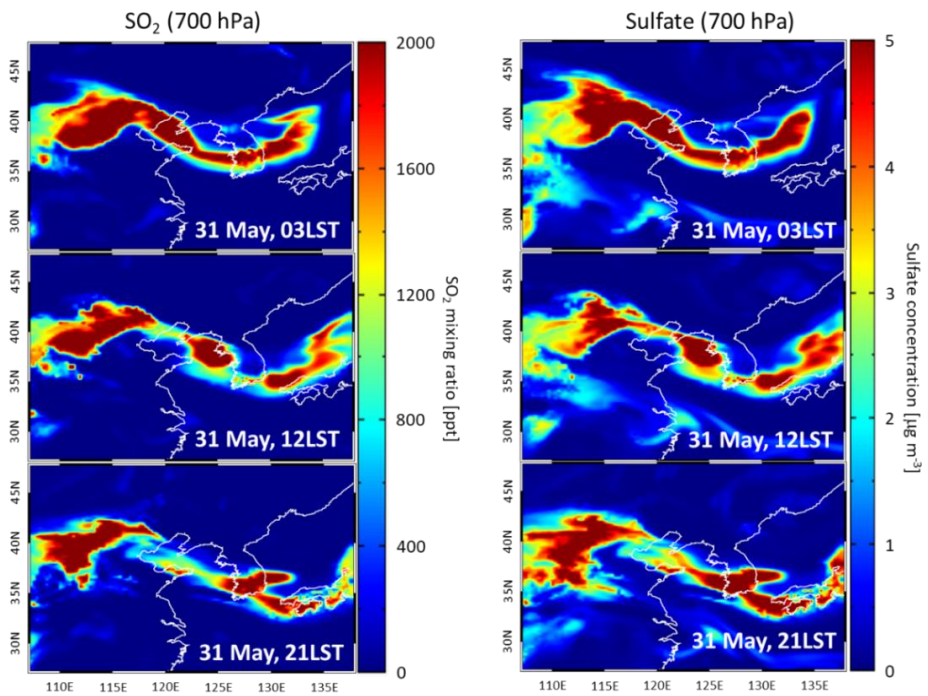

Figure 3.4. The spatial distribution of SO_2 mixing ratio (left panel) and sulfate concentration (right panel) at 700 hPa simulated by GEOS-Chem for FT NPF case (31 May, 2016).

To elaborate on the overall NPF characteristics during the KORUS-AQ campaign, the vertical profile of $N_{CN3\text{-}10}$ was examined. $N_{CN3\text{-}10}$ generally decreased with increasing altitudes, showing a peak of around 7,606 ± 12,003 cm^{-3} below 1 km altitude (**Fig. 3.5a**), suggesting NPFs around the Korean Peninsula were primarily regarded to occur in the BL rather than the FT. Previous studies reported that NPF frequency in the BL was highest during the springtime in the polluted urban area (Park et al., 2015) as well as relatively clean regional background sites (Kim et al., 2013). Furthermore, NPF occurrence rate during the KORUS-AQ campaign (~63%) was higher than the springtime seasonal mean (Lee et al., 2021), contributing to the BL peak of $N_{CN3\text{-}10}$ in this study. Although the NPF event was observed in the FT over the polluted areas such as urban Beijing and Yangtze River Delta region (Quan et al., 2017; Qi et al., 2019), the averaged vertical profile of $N_{CN3\text{-}10}$ over Korean Peninsula was more consistent to the results from the literatures that reported the active NPF in the BL (Väänänen et al., 2016; Altstädter et al., 2018).

$N_{CN3\text{-}10}$ was generally above 6,000 cm^{-3} up to the daytime BL height (~1 km) and rapidly decreased to about 3,000 cm^{-3} in the vicinity of 1 km altitude. $N_{CN3\text{-}10}$ decreased even more from an altitude of about 4 km, down to ~1,000 cm^{-3}. The number densities of aerosols with diameters from 10 nm to 199.5 nm were maintained over ~6,000 cm^{-3} from the

surface to the daytime BL height (**Fig. 3.5b**). A number density of ~3,000–4,000 cm^{-3} of accumulation-mode particles was observed at the 1–2 km range, possibly due to the influence of long-range transport of aged particles from upwind regions (Yu et al., 2006; Cho et al., 2021). Furthermore, particles in this size range (> 50–100 nm) can be potentially activated into CCN (Rose et al., 2017). This implied that the formation of low-level clouds below 2 km altitude can be highly influenced by vertical distribution of accumulation-mode particles over Korean Peninsula under low horizontal variability of activated CCN during the KORUS-AQ campaign (Park et al., 2020). Meanwhile, the number density of nucleation-mode (~15 nm) particles was over ~10,000 cm^{-3} near the surface, reflecting frequent particle formation in the BL.

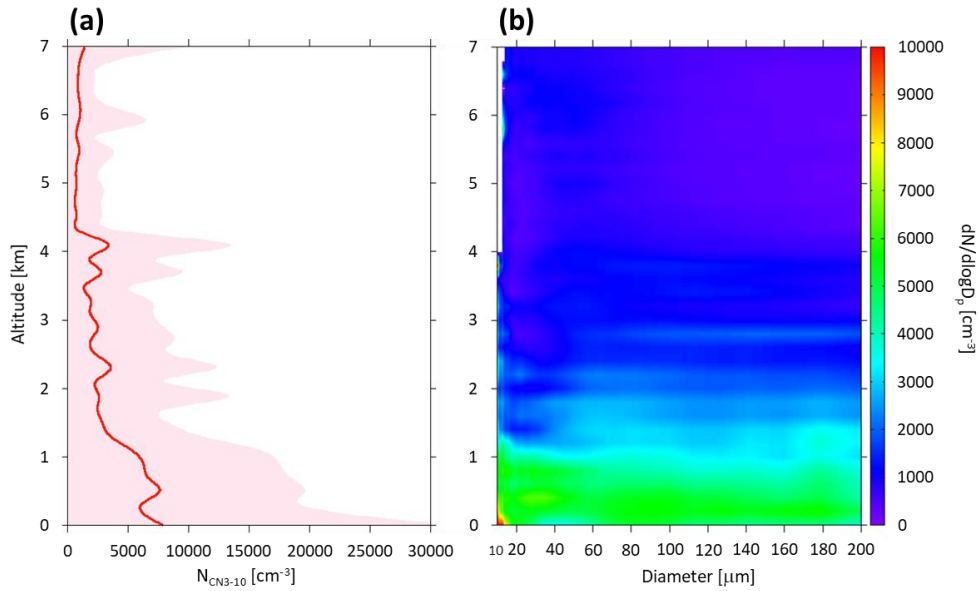

Figure 3.5. (a) The vertical profile of N_{CN3-10} during the KORUS-AQ campaign. The red line and pink shading denote the average and 1-standard deviation of N_{CN3-10}, respectively. (b) The vertical profile of number densities of aerosols with diameters from 10 nm to 199.5 nm during the KORUS-AQ campaign.

3.2 Evaluation of pandemic lockdown effect on the PNSD and NPF over Asian continental outflow

To evaluate the impact of the change in condensing vapors on the PNSD and NPF over Asian continental outflow, PNSD measured at three Korean background sites (Baengryeong (BRY) Anmyeon (AMY), and Jeju Bongseong (BOS)) during the LD period was analyzed. The PNSD at three background sites can be influenced not only by emissions from upwind continental regions but also by synoptic meteorological conditions in East Asia. **Figure 3.6** shows the spatial distribution of aerosol optical depth (AOD) and 850-hPa wind field during 2013–2019 and 2020. AOD is the monthly mean product estimated from Moderate Resolution Imaging Spectroradiometer (MODIS) Aqua platform, and wind vector was derived from NCEP/NCAR reanalysis 4-times daily data. Three sites located west of the Korean Peninsula were commonly affected by the long-range transport of aerosols from source regions in the Asian continent between 2013–2019 and 2020. The overall wind field during 2013–2019 was similar to that during 2020, except for the increased impact from the northerly wind in April. AOD levels in the source regions of the Asian continent from February to March generally decreased in 2020, implying a reduced transport of air pollutants toward the three sites (Zhang et al., 2021). In March 2020, the concentrations of air pollutants (e.g., $PM_{2.5}$, PM_{10}, NO_2, and CO) in the Korean Peninsula also

distinctly decreased in accordance with the strengthened social distancing policy of the South Korean government (Ju et al., 2021). In other words, the impact of the COVID-19 outbreak LD was prominent from February to March 2020. Because the Chinese LD was enforced from almost the end of January and the concentrations of pollutants (e.g., PM, O_3, NO_2, SO_2) rebounded in April (Fan et al., 2021), the meaningful COVID-19 LD period was set from February to March in this study.

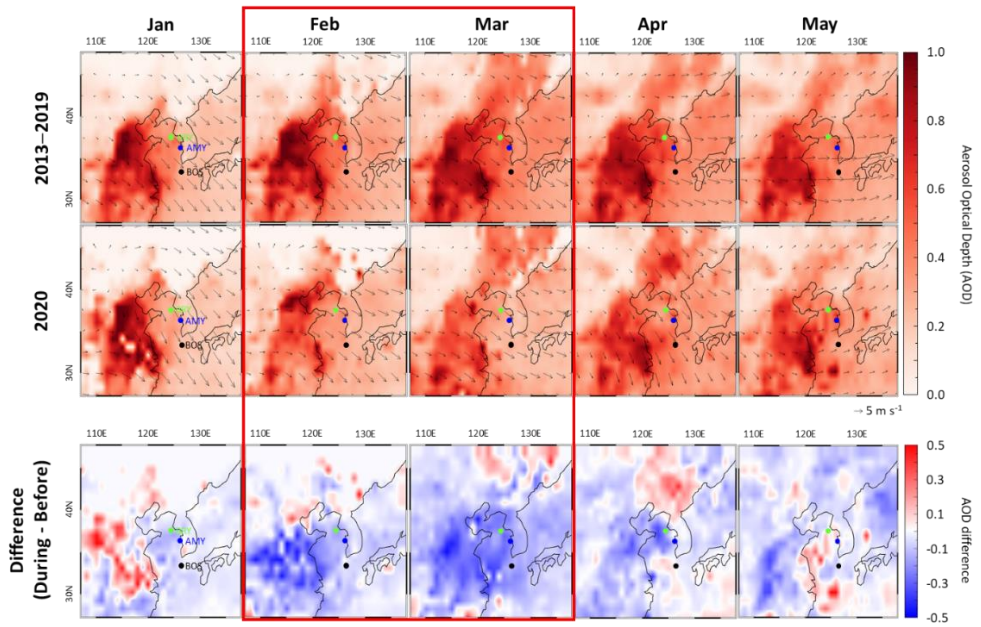

Figure 3.6. 850-hPa wind vector (arrow) from January to May during the period of 2013–2019 and 2020. The spatial distribution of AOD is represented as a color scale. Green, blue, and black circles denote the location of BRY, AMY, and BOS sites, respectively.

BRY showed a distinct decrease in the particle number concentration in both the nucleation and accumulation modes during the LD period. Although the PNSD according to diameter was not nearly unchanged, the number densities of aerosols decreased in all diameter ranges (**Fig. 3.7**). Among them, the number concentration of accumulation-mode particles (>90 nm; Kulmala et al., 2004) in the measurable size range decreased more (~34%) than that of nucleation-mode particles (<25 nm; Dal Maso et al., 2005; ~29%). The overall number concentration level in AMY during the Pre-LD period was the highest among the three regional background stations. In AMY, there was a negligible change in the number densities of aerosols, except for a slight decrease in the accumulation-mode particle number concentration in the afternoon. This was possibly due to the impact of precursor gases, including VOC emissions from industrial regions in the vicinity of the AMY site. Simpson et al. (2020) captured not only abundant VOCs such as toluene and benzene, but also significant formaldehyde, which is a product formed via photolysis of VOCs, at the Daesan petrochemical complex near the AMY station based on observations from the Korea-United States Air Quality Study (KORUS-AQ) campaign in 2016. Furthermore, the decrease in $PM_{2.5}$ concentrations in the cities in South Korea during the social distancing led by the South Korean government (from February 29, 2020) were positively correlated with the $PM_{2.5}$

emission fraction for mobile sources but negatively correlated with the combustion and industrial sources (Kwak et al., 2021). From these reports, the artificial reduction in industrial emissions was expected to be not significant during the period of social distancing in South Korea. The diurnal pattern of the PNSD at the BOS site had the characteristics of a high-altitude station. The number densities of particles were significantly lower than those at the BRY site during the nighttime because of the decay of the nocturnal marine boundary layer. The long-lasting enhancement of nucleation-mode particles (~16 local standard time (LST)) at the BOS site compared to that at the other sites was likely influenced by the transportation of gaseous precursors or nanoparticles following the daytime valley wind until the afternoon (Bei et al., 2018; Park et al., 2018). Furthermore, the impact of emission changes from the source regions in the Asian continent can be weaker at the BOS because of its higher altitude. The PNSD in the BOS site over the LD period also experienced a decrease in number concentration in both the nucleation and accumulation modes; however, its magnitude (11% and 24% in the nucleation and accumulation modes, respectively) was lower than that of the BRY site.

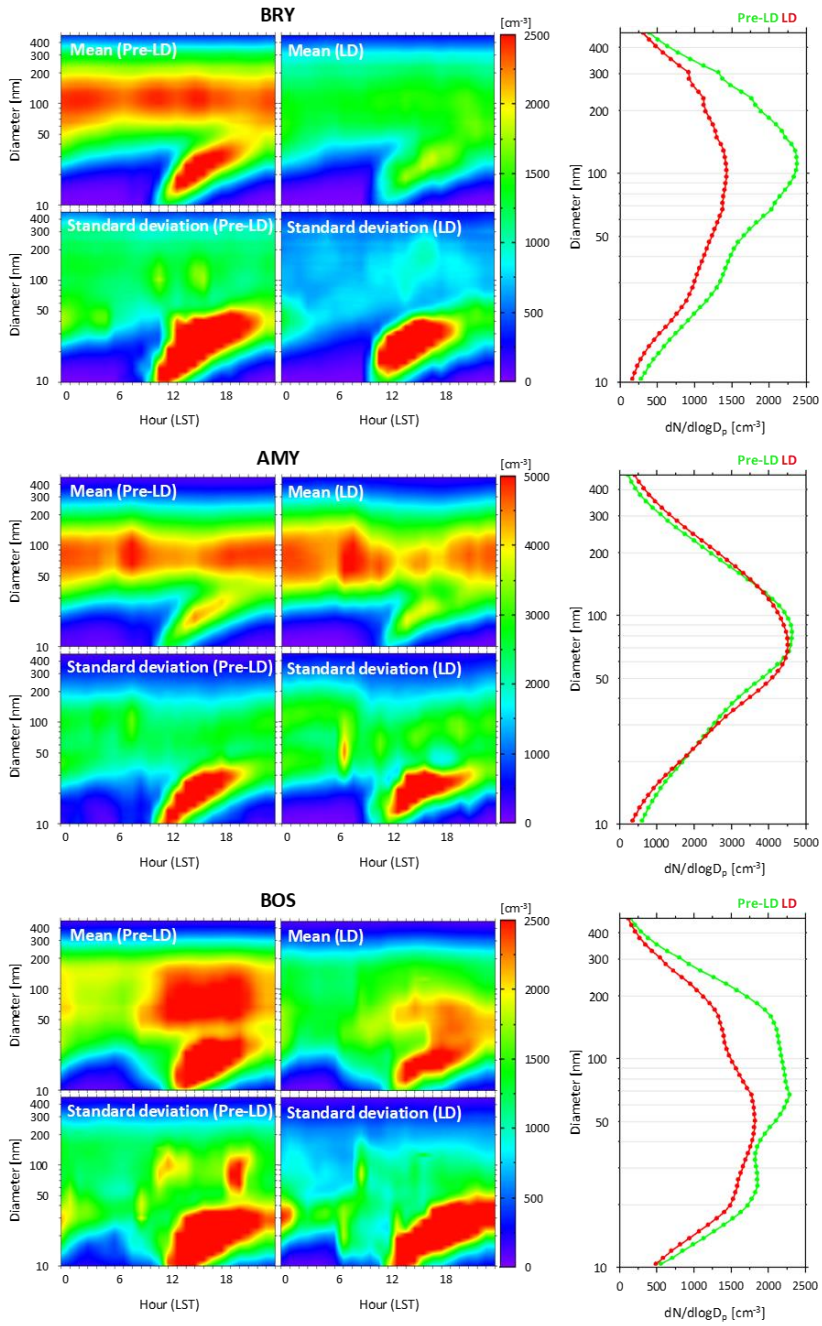

Figure 3.7. (a) Diurnal variation in mean PNSD and its standard deviation in three sites during the Pre-LD (left) and LD (right) periods. (b) Mean size distribution from 10–469.8 nm in the Pre-LD (green) and LD (red) periods.

The CSEOF technique was applied to the daytime (7–16 LST) PNSD dataset measured at the three sites during the study period (Kim et al., 2013; Kim et al., 2021; Park et al., 2021b). All mode 1 CSLVs corresponded to typical NPF and subsequent growth, accounting for 34%, 27%, and 35% of the total variance of the PNSD measured at the BRY, AMY, and BOS sites, respectively (**Fig. 3.8a**). Particularly, mode 1 CSLVs at the BOS site also included a positive anomaly in the number concentration of accumulation-mode particles. Unlike the other two sea level sites, the daytime CSLV mode 1 at the BOS site can show a significant positive anomaly in the accumulation-mode as well as nucleation-mode size range under cloud-free clear weather conditions because it is a favorable condition for NPF as well as the development of the marine boundary layer (Hamed et al., 2007) or daytime valley breeze (Lehner et al., 2019). Specifically, when NPF occurs under the clear weather condition, not only the development of a marine boundary layer due to the intense solar heating can expand the well-mixed region up to the altitude of BOS, but also an active valley breeze can bring the aerosols up to the BOS as well.

Since mode 1 CSLVs corresponded to the typical diurnal patterns during regional NPF events (Kerminen et al., 2018), NPF events were identified based on the CSEOF mode 1 PC amplitudes. NPF events were

identified using the daytime PC amplitudes for February–March during the entire study period from 2013 to 2020. If the PC amplitudes were lower than zero, the day was classified as a non-NPF event. Moreover, strong- and weak-NPF events were distinguished based on the threshold value calculated by averaging the positive daytime PC amplitudes for each site (**Fig. 3.8b**; Kim et al., 2013).

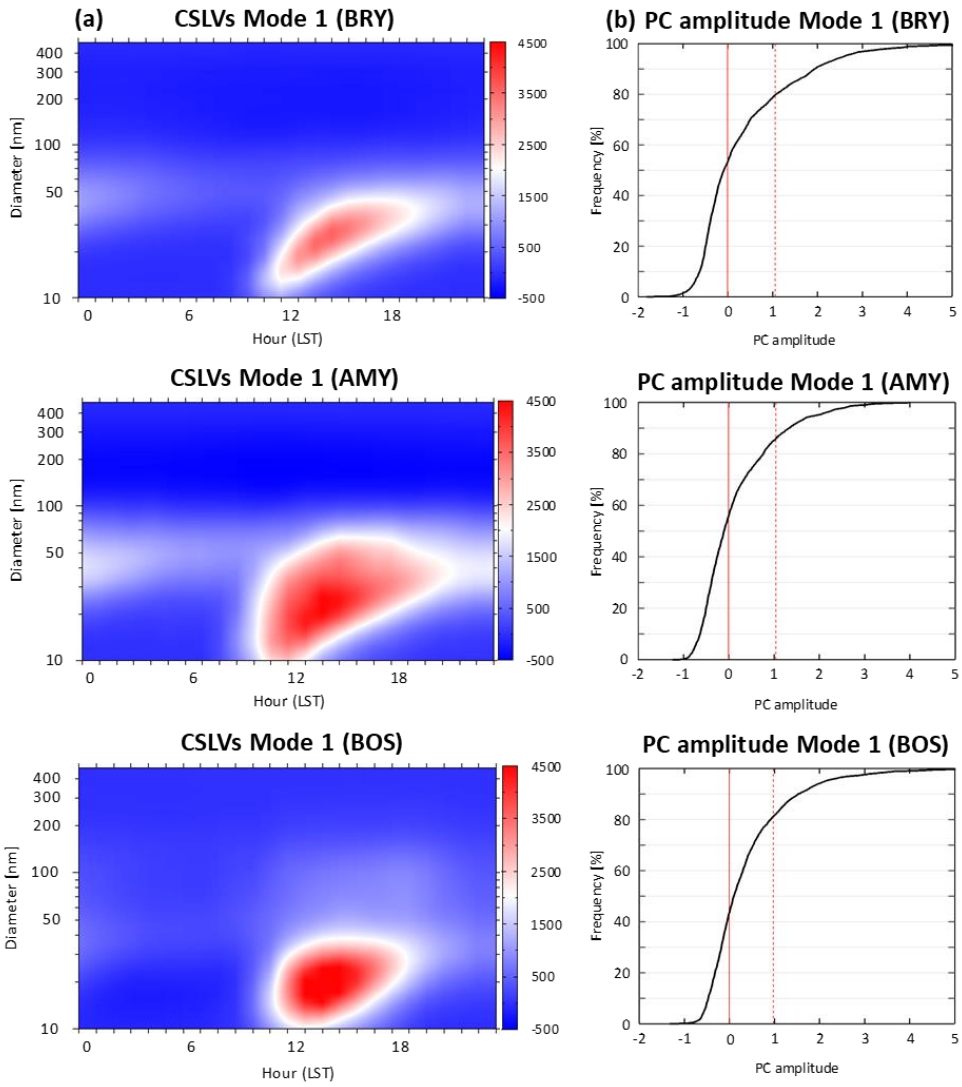

Figure 3.8. (a) Cyclostationary loading vector of first CSEOF mode (Mode 1 CSLVs) calculated from the PNSD obtained at the BRY, AMY, and BOS sites. (b) Cumulative frequency for the daytime (7–16 LST) CSEOF mode 1 PC amplitude for February–March during the study period (2013–2020). The zero line and a threshold value for distinguishing weak- and strong-NPFs are represented as solid red and dashed lines, respectively.

An average PNSD profile of strong-, weak-, and non-NPF for the entire study period is presented in **Figure 3.9**. The diurnal variation in PNSD during the strong-NPF events showed a distinct so-called 'banana-plot' at all sites. The clear banana shape on the plot of PNSD with time shows the features of regional NPF, which is distinguished from sub-regional NPF events that capture only a partial banana shape on the PNSD plot (Kerminen et al., 2018). During weak-NPF events, a relatively moderate increase in the number concentration of nucleation-mode aerosols was observed near noon. The number of aerosols in the growing mode was also significantly lower than that during strong-NPF events. Meanwhile, the enhancement of the nucleation-mode particles was nearly negligible during non-NPF events.

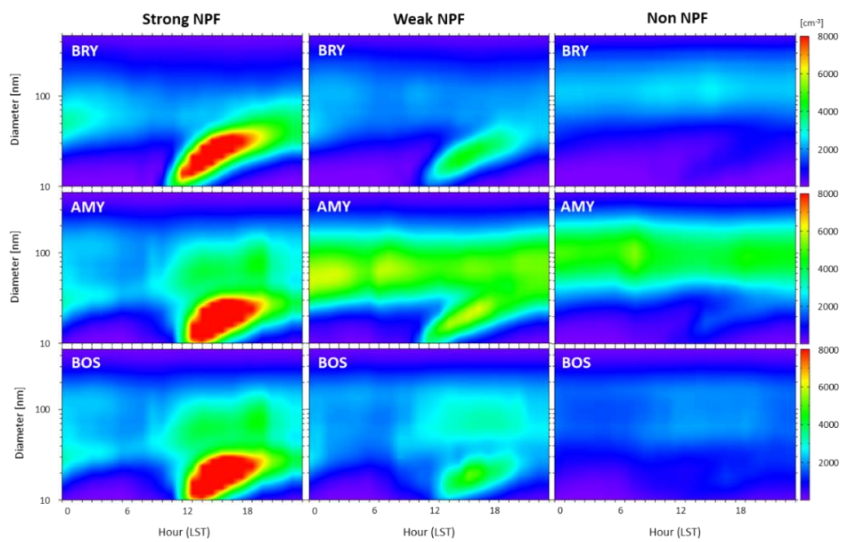

Figure 3.9. Averaged diurnal variation in PNSD during the classified strong- (left), weak- (middle), and non- (right) NPFs at the three sites.

The CSEOF-based classification used in this study captured typical PNSD characteristics on NPF days. **Figure 3.10** shows an example of the classification result in February 2017 in BRY, where five days (February 1, 6, 11, 17, and 23) and three days (February 9, 20, and 21) were identified as strong-NPF and weak-NPF events, respectively. In particular, only February 9 and 11 were classified as weak- and strong-NPF events during 8–11 February. The CSEOF technique distinguished NPF days based on the objective numerical amplitude of diurnal PNSD evolution, even though this period was somewhat ambiguous in terms of NPF identification. The distinct increase in nucleation-mode particles near the lowest diameter (~10 nm) could be the most important for being classified as an NPF event based on the classification result. February 8 and 10 could be regarded as days influenced by the transport of slightly aged newly-formed fresh particles (~20–30 nm) from the vicinity of the station. The identification of NPF events using the CSEOF technique also has been validated in the previous study (Kim et al., 2013).

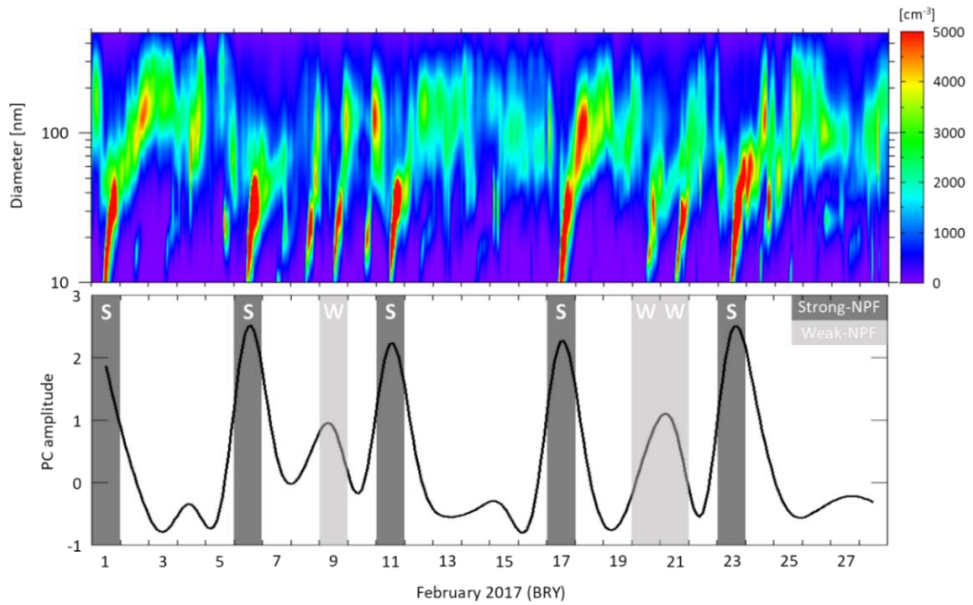

Figure 3.10. (Upper) Monthly variation in PNSD measured at BRY in February, 2017. (Lower) Monthly variation in daytime-averaged (7–16 LST) time series of PC amplitude and classification results.

The change in NPF events during the COVID-19 LD period was investigated in terms of frequency based on the previously shown NPF classification method. The frequencies of NPF (i.e., the sum of strong- and weak-NPF events) in BRY, AMY, and BOS during the Pre-LD period were 40%, 37%, and 46%, respectively (**Fig. 3.11**). The NPF frequencies estimated at the sea-level sites (BRY (40%) and AMY (37%)) in this study were lower than those determined by applying the method suggested by Dal Maso et al. (2005) to the PNSD observed at a rural background site located downwind of the Seoul metropolitan area during the spring

season (52%; Lee et al., 2021). However, our results were closer to those estimated by applying the objective numerical value to the number concentration of 20-nm aerosols for NPF classification, which reported approximately 32% for March-April in AMY (Matsui et al., 2013). As BOS can be frequently located above the shallow marine boundary layer during the night, it can be in a clean environment in the early morning without aged particles, which play a role as the sink of newly-formed fresh particles, resulting in a relatively higher NPF frequency compared to other sites. Several previous studies have also reported a substantial frequency of NPF events associated with upslope valley winds in mountainous locations (Kerminen et al., 2018). Higher frequencies were observed than those in BOS at the high-altitude sites, such as Chacaltaya, during the dry season (64%; Rose et al., 2015) and the Storm Peak Laboratory (52%; Hallar et al., 2011; 2016).

During the LD in 2020, NPF frequency decreased by 7%, 1%, and 7% in BRY, AMY, and BOS, respectively. As a strict classification of NPF, it is also worth examining the change in strong-NPF frequency during the LD period. The decrease in strong-NPF events mainly led to a decline in the entire NPF frequency, with 6% (BRY), 2% (AMY), and 5% (BOS) decreases. The proportion of strong-NPF events among all NPF events also significantly decreased at all sites during the LD period (48% to 38%

in BRY, 34% to 24% in AMY, and 31% to 24% in BOS). The less frequent occurrence of NPF events during the LD period is discussed later in this section.

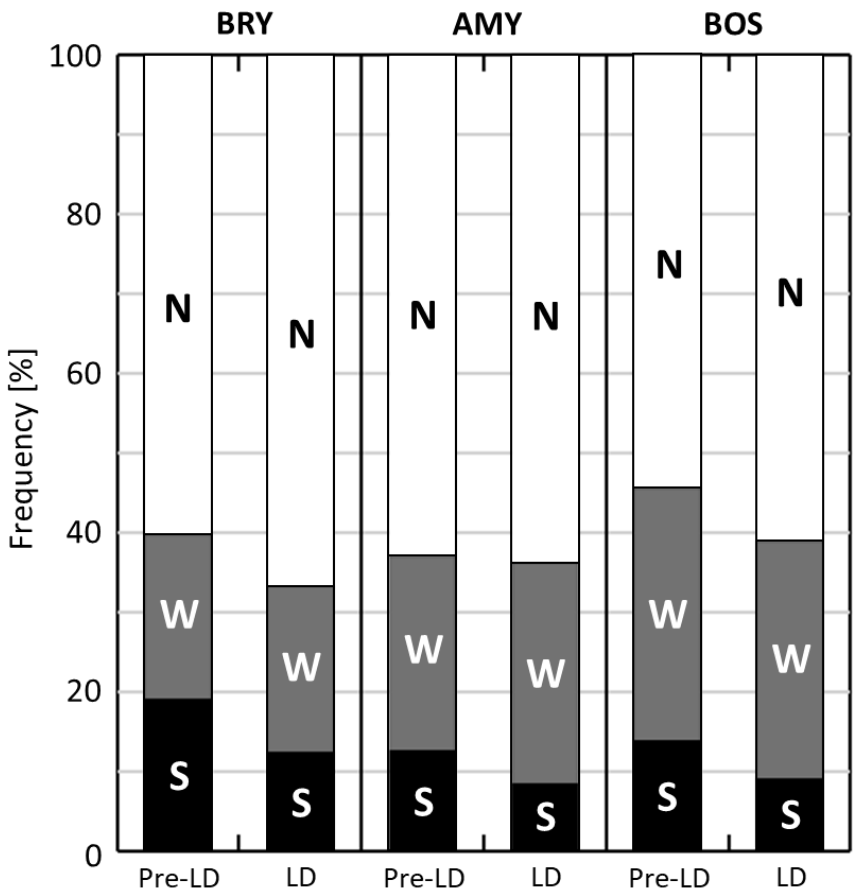

Figure 3.11. (a) Frequency of strong- (black), weak- (gray), and non- (white) NPF events during the Pre-LD and LD periods at the BRY, AMY, and BOS sites.

Because meteorological conditions are known to significantly influence the occurrence of NPF events (Bousiotis et al., 2021), changes

in meteorological conditions were also investigated during the NPF occurrence time (8–12 LST; Tang et al., 2021) of the LD period (**Table 3.1**) using data from the Automated Synoptic Observing System produced by the Korea Meteorological Administration. Although diverse physical processes associated with ambient temperature can promote or suppress the occurrence of NPF (Kerminen et al., 2018), biogenic aerosol precursor vapors can be more actively emitted into the atmosphere with increased ambient temperature, promoting the occurrence of NPF and subsequent growth (Debevec et al., 2018). Although H_2O can participate in the formation of initial clusters via binary or ternary nucleation (Yao et al., 2018), increased RH reduces the probability of fresh particles surviving by producing a larger aerosol surface area (Li et al., 2019; Wu et al., 2019). A higher wind speed (WS) can create favorable conditions for the occurrence of NPF events by eliminating pre-existing particles (Pushpawela et al., 2019). Increased solar radiation can promote photochemical gas-phase reactions and ultimately contribute to the production of condensable vapors in NPF (Boy and Kulmala, 2002).

Because of the absence of solar radiation measurements in AMY and BOS, meteorological data measured in Seosan (SS; 36.78°N, 126.49°E) and Gosan (GSN; 33.29°N, 126.16°E) were used, respectively. In addition, it is worth noting that insolation measurement in BRY began in 2019.

Generally, meteorological changes appeared at all three stations during the LD period, showing unfavorable changes (i.e., an increase in RH or decrease in WS) and a favorable change (an increase in ambient temperature) for NPF occurrence. However, several previous studies reported that the negative impact of increased RH on NPF occurrence becomes small in the range of RH at these sites (61% in BRY and 67% in GSN during the Pre-LD period; Wu et al., 2019; Figure 4 in Bousiotis et al., 2021). Furthermore, Pushpawela et al. (2019) reported that the impact of WS change on the NPF frequency decreased in rural regions owing to the low number of pre-existing particles ventilated by the wind. Meanwhile, variations in insolation during the LD period were not statistically significant at any of the three sites, suggesting that photochemical reactions for NPF occurrence were not meaningfully promoted or suppressed by the insolation change. In other words, all three sites showed decreased NPF frequency under the reduced emission of precursor gases from the source regions in the Asian continent during the LD period, despite favorable meteorological conditions for NPF occurrence mainly developing by increased temperature.

Table 3.1. Variations in NPF occurrence time (8–12 LST) surface meteorological factors during the LD period at three sites. Values in the parenthesis represent the difference in each meteorological factor between the LD and pre-LD periods. When the difference is statistically significant, the impact of meteorological variation on NPF occurrence is reflected in the background color in each compartment in the table.

Promotion of NPF occurrence
Suppression of NPF occurrence

	BRY	AMY (SS)	BOS (GSN)
Temperature (˚C)	↑ (+4.85)	↑ (+3.39)	↑ (+3.39)
Wind Speed ($m\ s^{-1}$)	– (-0.09)	↓ (-0.29)	↓ (-0.76)
RH (%)	↑ (+12.95)	– (-2.35)	↑ (+6.41)
Insolation ($MJ\ m^{-2}$)	– (-0.14)	– (+0.08)	– (-0.14)

Considering the substantial contribution of inorganic components to the particulate matter in East Asia (Jordan et al., 2020), the production of sulfuric acid (H_2SO_4) is crucial to the occurrence of NPF events. Because gaseous SO_2 plays a dominant role in the formation of H_2SO_4 via photochemical reactions in the presence of ultraviolet (UV) radiation, the UV multiplied by the SO_2 mixing ratio can be used as a surrogate for the H_2SO_4 concentration when this value is considered together with the condensation sink (CS) (Petäjä et al., 2009; Dall'Osto et al., 2018). In this study, hourly maximum solar radiation in the UV-B range ($W\ m^{-2}$) was used, considering that, UV-B mainly contributes to the photolysis of

ozone and is ultimately related to the formation of hydroxyl radicals ($^{\bullet}OH$). The condensation sink (s^{-1}), which can be an indicator of the condensation rate of non-volatile gaseous compounds on pre-existing large particles, was obtained following the method introduced by Kulmala et al. (2001). In this study, SO_2 mixing ratio was measured in BRY, Pado-ri located close to the AMY station (~8 km away from AMY), and GSN. Additionally, UV-B measurements were conducted in Incheon (INC; 37.48 °N, 126.6249 °E), AMY, and GSN. Owing to the absence of UV-B measurements in BRY, data measured at INC from February–March of 2018 (4,272 hourly data) were used to represent the H_2SO_4 proxy in BRY despite the substantial distance, considering the relatively homogeneous spatial distribution compared to the properties of gaseous pollutants. Except for BRY, UV-B measured from February–March 2013 (11,376 hourly data) was analyzed. SO_2 mixing ratio and UV-B intensity (in parenthesis) for the study period were 1.6±0.9 ppb (0.0496±0.0376 W m^{-2}), 2.2±1.5 ppb (0.0449±0.0398 W m^{-2}), 0.7±0.7 ppb (0.0496±0.0461 W m^{-2}) in BRY, AMY, and BOS, respectively. Generally, UV-B intensity during the NPF events was significantly lower than that during the non-NPF events ($p << 0.05$) at all three sites, but it was not the case for the SO_2 mixing ratio in the low-level stations (BRY and AMY). According to the brief sensitivity test for the NPF frequency with the increasing lower

limit of the UV-B intensity from 0 to 0.15 W m^{-2}, NPF frequency increased from 36% to 50% in BRY, 37% to 49% in AMY, and 45% to 54% in BOS, suggesting UV-B intensity is closely connected to the occurrence of NPF.

Figure 3.12 shows the diurnal variation in the H_2SO_4 proxy ([UV-B radiation intensity] × [SO_2 mixing ratio]; ppb W m^{-2}) during the NPF and non-NPF events over the Pre-LD and LD, respectively. The H_2SO_4 proxy was generally the highest near noon at all the three sites, implying a more significant contribution of inorganic compounds to the formation of new particles over time during the NPF occurrence time (8–12 LST). The H_2SO_4 proxy estimated at the three sites during the NPF occurrence time significantly decreased over the LD period. Under these circumstances, the H_2SO_4 proxy during 8–12 LST was higher during the NPF events compared to non-NPF events over both the Pre-LD and LD at the AMY and BOS sites. Thus, the decrease in NPF frequency in BOS and AMY can be attributed to the reduced H_2SO_4 proxy during the LD period. However, BRY did not show a statistically significant difference in the H_2SO_4 proxy between the NPF and non-NPF events over both the Pre-LD and LD periods ($p \approx 0.12$, pre-LD; $p \approx 0.60$, LD). This indicates that the H_2SO_4 proxy can be saturated for the occurrence of NPF and is not a determining factor for NPF. The H_2SO_4 proxy relative to CS ([H_2SO_4 proxy]/[CS]) during the NPF occurrence time was the highest in BRY (13.684 ± 13.715

ppb W m^{-2} s), followed by AMY (11.789 ± 16.657 ppb W m^{-2} s) and BOS (7.546 ± 9.870 ppb W m^{-2} s).

The BRY region can be more susceptible to being influenced by the emission changes in hotspot regions in the Asian continent because of its lower altitude and the absence of local emissions compared to other sites. Although the altitude of AMY is lower than that of BRY, they are typically located in a vertically well-mixed marine boundary layer during February–March (Takegawa et al., 2020). Several works have reported that the emission changes in organic gaseous precursors for NPF are also significant. For example, Shen et al. (2021b) reported that most VOCs measured in urban Beijing decreased during the Chinese LD period, except for benzene. Although the formation efficiencies of secondary aerosols increased during the LD period under the enhanced atmospheric oxidation capacity, a reduction in the mass concentration of organic aerosol factors during the LD period was also captured by Tian et al. (2021). The decrease in the NPF frequency estimated in BRY can be highly influenced by the reduction in anthropogenic low-volatile organic precursors emitted from upwind regions.

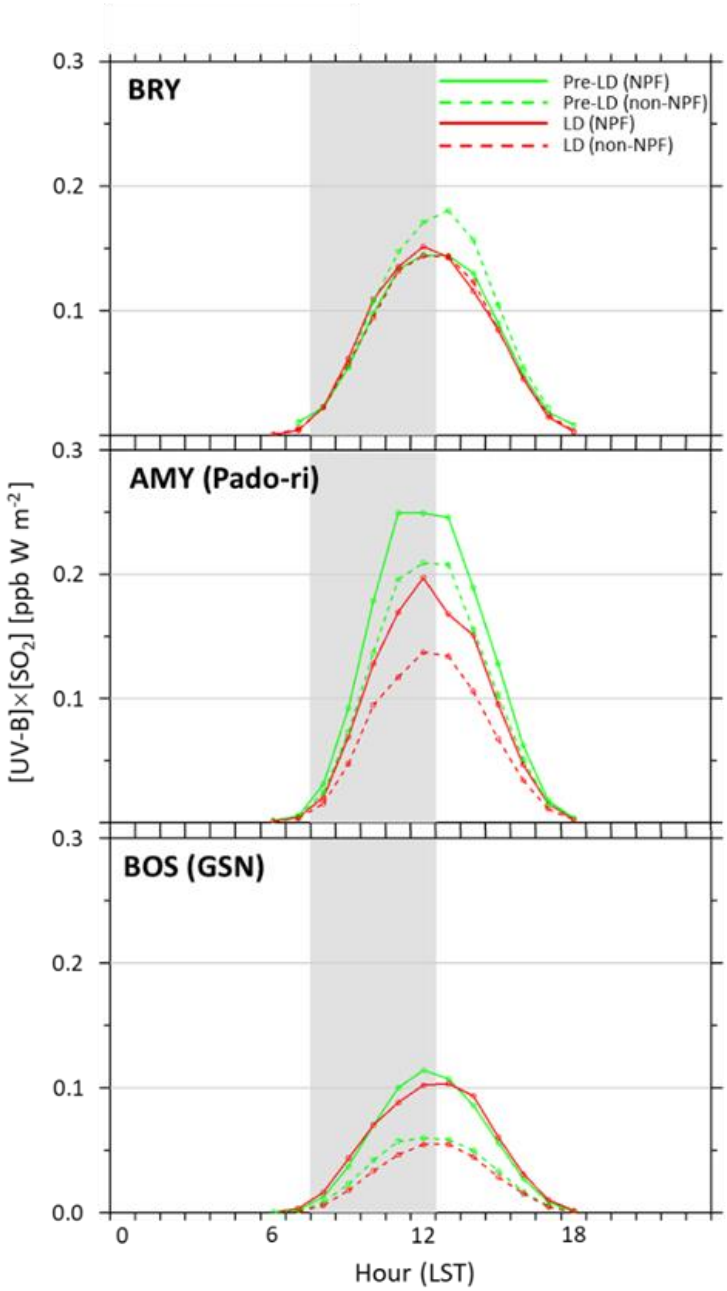

Figure 3.12. Diurnal variation in H_2SO_4 proxy at the BRY, AMY, and BOS sites during the Pre-LD (green) and LD (red) periods. Diurnal variation during the NPF (Strong- and Weak-NPF) events and non-NPF events are represented as solid and dashed lines, respectively. NPF occurrence time (8–12 LST) is the shaded area.

Since the 2010s, anthropogenic pollutant emissions in East Asia have steadily declined. For example, the decreasing trend of SO_2 and NO_x emissions was identified, which was motivated by measures such as levying an environmental protection tax (Sun et al., 2018). Therefore, the sharp reduction in pollutant emissions due to LD measures provided an observation-based natural experiment for the investigation of the NPF properties in the future atmosphere under these trends of condensing vapors acting as precursors. Based on the results of this study, policy strategies would be more systematically established to prevent the future occurrence of puzzling haze events originating from NPF.

Chapter 4. Trend analysis of PNSD and NPF on the global scale

4.1 Elaboration on the environmental characteristics from multi-year PNSD observation from in-Situ Aerosol Global Atmosphere Watch Network (SARGAN)

The PNSDs are highly influenced by regional atmospheric NPF depending on its different frequency and intensity (FR & GR) according to each environment (Nieminen et al., 2018; Rose et al., 2021). Because the temporal and spatial variability for the regional NPF and PNSD can be quite substantial, it is necessary to conduct integrated global analysis of them. Although spatial/seasonal variability of CN, PNSD, and NPF were documented by Laj et al. (2020), Rose et al. (2021), and Nieminen et al. (2018) using the global data whose time span is longer than a year, more solid environmental elaboration of PNSD would be conducted based on the multi-year measurement enough to capture long-term trend in this section, because long-term observations in a lot of stations worldwide have been secured up to the present. Among the sites operating MPSSs to derive PNSD data in in-Situ AeRosol GAW Network (SARGAN), lowland sites with available long-term (> 5 years) continuous data were selected, excluding mountain sites. The classification between mountain and lowland was conducted by examining data description in raw data, Rose et al. (2021) and previous studies listed in the **Table 4.1**. Finally, 27

lowland sites were selected, being subdivided for 8 of urban, 15 of rural, and 4 of remote sites. Urban stations generally have clear anthropogenic emission sources, but remote sites are dominated by pollutants emitted by natural sources. In this study, rural region is defined as a region which can be influenced by anthropogenic emissions from upwind regions according to the favorable conditions for the transport of atmospheric pollutants, despite the absence of the local emission sources. For consistency, colors in all the figures in this section were represented as red for urban, green for rural, and blue for remote sites, as displayed on **Table 4.1**.

Comprehensive descriptions for 27 selected lowland stations were represented in **Figure 4.1** and **Table 4.1**. Because aerosol physical properties have been actively monitored in European stations under the systematic observation networks such as Aerosols, Clouds and Trace gases Research Infrastructure (ACTRIS), many stations are located in European regions. This spatial bias can be limitation of the analysis, provoking systematic MPSS measurement associated with more broad spatial coverage under solid observation network. This study concentrated on the contrast of PNSD and NPF characteristics according to the different observation environments, rather than explaining characteristics or trend based on the spatial distribution. For the

measurement, lower/upper size limits of PNSD observation were different according to the sites and observation periods. For example, PNSD was derived for wide size range (3–1000 nm) for HYY, while only PNSD from 6 to 389 nm was obtained in ASP. Actually, distribution of size bins was typically different with the period of observation in a single station, because this study uses all available PNSD data whose time span is up to 25 years. To handle this issue in a consistent manner, most narrow size range was selected as a standard and the data measured in a rest of the period were interpolated to the standard composition of size bin.

In terms of NPF, lower size limits for the PNSD derivation among the sites should be discussed. Although KUM, HYY, VAV, and VAR can identify NPF signals from PNSD diurnal profile by directly capturing 3-nm particles which are similar to freshly formed molecular clusters, there are many stations operating MPSSs whose lower size limits are about ~10 nm. According to Kerminen et al. (2018), although the formation of molecular clusters takes place anytime and everywhere in the ambient atmosphere, nanoparticle formation grown by homogeneous or heterogeneous nucleation occurs only under favorable atmospheric conditions such as intense solar radiation and low relative humidity (Kulmala et al., 2014). Several previous literatures reported that the

growth rate of sub-10 nm particles is larger than a few nm h^{-1}. For example, Vana et al. (2016) reported that the growth rate in size range of 3–7 nm was 3.7–2.0 nm h^{-1} and 3.8–2.6 nm h^{-1} for positive and negative ions, respectively, based on the measurement conducted in Hyytiälä station during 2013–2014. Although there is a large amount of low-volatile biogenic emission significantly contributing to the particle growth in Hyytiälä, time scale (~1–2 hours) for newly formed particles to reach 10-nm size can be not much different from that estimated in urban regions, considering that substantial level of sulfuric acid participating in the initial stage of the particle growth, accounting for up to ~60% of particle growth in urban Beijing (Yue et al., 2010). Once the favorable atmospheric conditions for NPF occurrence are built up, MPSSs of those stations can capture the newly formed particles within a short time when the precursor concentrations and atmospheric conditions are hard to be sharply changed. Naturally, so-called 'banana' shape in the diurnal variation of PNSD plot can be a signal from the growth of particles formed at the exterior of the measurement site. Although that can be the case, the banana-shape in the PNSD plot is an evidence for the regional NPF whose spatial scale is about hundreds of kilometers, according to Kerminen et al. (2018). Sub-regional NPF caused by coal-fired plants or biomass burning can be represented as only a partial banana-shape in the diurnal variation of the PNSD plot. Thus, nanoparticles smaller than

~10 nm is not likely to be transported from other remote regions, considering the spatial scale of the general regional NPF as well as the growth rate of sub-10 nm particles stated above.

Because of these properties of regional NPF, lower size limit of nucleation-mode particles was set to be 10 nm. NPF frequency estimated from SMPS having a lower size cut of ~10 nm was also analyzed in several previous studies (e.g., Kim et al., 2014; Nieminen et al., 2018). Especially, Nieminen et al. (2018) documented the NPF frequency using the lower size cut of ~10 nm around the world. Although upper size limit of nucleation-mode particles can be selected diversely according to the research objectives, it was selected as 25 nm because flux of particles out of nucleation-mode size range by particle growth can be ignored when NPF intensity (e.g. particle formation rate) is calculated (Kerminen et al., 2018). This upper limit is also selected in the work of Nieminen et al. (2018).

Overall, total number concentration (10–500 nm) was highest in urban sites, being followed by rural and remote regions. In detail, DRN and LEI-E shows especially high value in total number concentration under the impact from vehicle exhaust because they are roadside stations. Total number concentration measured in DRN shows clear difference with DRW, while LEI-E is even lower than LEI-M. Generally, Overall,

particle number concentration level was several thousands of cm^{-3} in urban and rural sites, but showed only several hundreds of cm^{-3} in remote sites except for FKL.

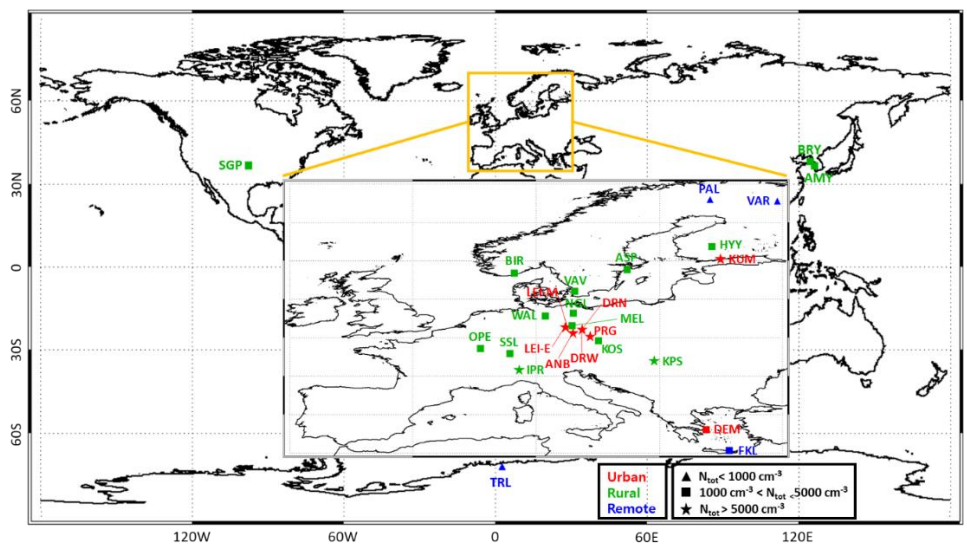

Figure 4.1. The location of measurement stations with PNSD data. The shape and color of station markers indicated the range of total aerosol number concentrations and observation environment, respectively.

Table 4.1. Comprehensive descriptions of 27 selected lowland sites.

Environment	Station	Abbrev.	Coordinates	Alt. (m)	Period	Size range (nm)	Total number conc. (cm^{-3})	References
Urban	Annaberg_Buchholz	ANB	50°34′N, 13°00′E	545	2012–2020	10–800	6284±3791	Schladitz et al. (2015)
	DEM_Athens	DEM	37°59′N, 23°48′E	270	2015–2020	10–550	4513±3391	Vratolis et al. (2019)
	Dresden_Nord	DRN	51°03′N, 13°44′E	120	2001–2020	5–800	14718±9674	Atzler et al. (2022)
	Dresden-Winckelmannstrasse	DRW	51°02′N, 13°43′E	112	2010–2020	10–800	6297±3069	Atzler et al. (2022)
	Kumpula	KUM	60°12′N, 24°57′E	25	2006–2020	3–794	5789±3581	Hussein et al. (2014)
	Leipzig-Eisenbahnstrasse	LEI-E	51°21′N, 12°24′E	111	2011–2020	10–800	10353±4152	Sun et al. (2019)
	Leipzig-Mitte	LEI-M	51°20′N, 12°22′E	111	2010–2020	10–800	11492±4278	Birmili et al. (2013)
	Prague-Suchdol	PRG	50°07'N, 14°23'E	270	2012–2020	10–519	6411±3779	Skrabalova et al. (2015)
Rural	Anmyeon	AMY	36°32'N, 126°19'E	46	2013–2020	10–470	3770±1474	Park et al. (2023)
	Aspvreten	ASP	58°48'N, 17°23'E	20	2000–2017	6–389	2026±1009	Tunved et al. (2019)
	Birkenes II	BIR	58°23′N, 8°15′E	219	2009-2020	10–550	1540±1108	Aas et al. (2019)
	Baengryeong	BRY	37°57′N, 124°37′E	135	2013–2020	10–470	1821±890	Park et al. (2023)
	Hyytiälä	HYY	61°51′N, 24°17′E	181	1996–2020	3–1000	1932±1119	Kulmala et al. (2022)
	Ispra	IPR	45°48′N, 8°38′E	209	2008–2020	10–600	7397±3326	Shen et al. (2021a)
	Kosetice (NOAK)	KOS	49°34′N, 15°04′E	535	2008–2020	5–800	3645±2084	Zíková et al. (2013)
	K-puszta	KPS	46°58′N, 19°35′E	125	2006–2020	6–794	5188±2207	Molnár et al. (2016)
	Melpitz	MEL	51°31′N, 12°55′E	86	1996–2020	5–800	4613±2067	Größ et al. (2018)
	Neuglobsow	NGL	53°10'N, 13°02'E	62	2011–2020	10–800	3354±1523	Heintzenberg et al. (2018)
	Obs. Perenne de l'Environnement	OPE	48°33'N, 5°30'E	392	2013–2020	10–544	2378±1285	Farah et al. (2020)
	Southern Great Plain	SGP	36°36'N, 97°29'W	318	2016–2020	11–461	2527±1193	Marinescu et al. (2019)
	Schauinsland	SSL	47°54'N, 7°55'E	1205	2005–2020	10–800	2198±1375	Leinonen et al. (2022)

Table 4.1. Continued.

Rural	Vavihill	VAV	56°01'N, 13°09'E	175	2001–2017	3–858	4031±4360	Kristensson et al. (2008)
	Waldhof	WAL	52°48'N, 10°45'E	74	2009–2020	10–800	3986±1875	Heintzenberg et al. (2018)
Remote	Finokalia	FKL	35°20′N, 25°40′E	150	2009–2020	9–849	2508±1163	Kalkavouras et al. (2020)
	Pallas	PAL	67°58'N, 24°06'E	565	2000–2020	7–493	660±1176	Mielonen et al. (2013)
	Trollhaugen	TRL	72°00′S, 2°32'E	1309	2016–2020	10–800	326±346	Rose et al. (2021)
	Värriö	VAR	67°46'N, 29°35'E	400	2000–2020	3–708	794±747	Vana et al. (2016)

To understand environmental characteristics of NPF frequency and intensity (FR & GR), NPF events were distinguished from non-NPF events by applying CSEOF technique stated at previous section on the observed PNSD from 10 nm to 300 nm. Using PNSD measurement in HYY, an example of the NPF identification (May 8–14, 2018) was displayed on **Figure 4.2**. In this example (**Fig. 4.2a**), May 8–11 were classified as strong-NPF and May 12 was weak-NPF event. From the example, distinct enhancement of number concentration of particles whose diameter is close to lower size limit was a key factor for a day to be classified as strong-NPF event. For weak-NPF event, the number densities of aerosols are lower than those in strong-NPF days, although clear banana-shape on the diurnal pattern of PNSD was maintained. CSLVs of mode 1 for 25-year measurement represented also typical diurnal pattern during the regional NPF, which was similar to those in Korean background sites, accounting for 31.8% of the PNSD variance. (**Fig. 4.2b**). All averaged PNSD for strong-, weak-, and non-event days, the magnitude (~5000 cm^{-3}) of the peak was largest as well as the location of the peak diameter was smallest (~36 nm) during the strong-NPF days (**Fig. 4.2c**). Although most of the previous works applied NPF classification proposed by Dal Maso et al. (2005), global NPF analysis in this study was conducted based on the CSEOF technique because this method uses more objective value for PC amplitude, and automatic for detecting NPF events from a

significantly large period of data measured from numerous stations.

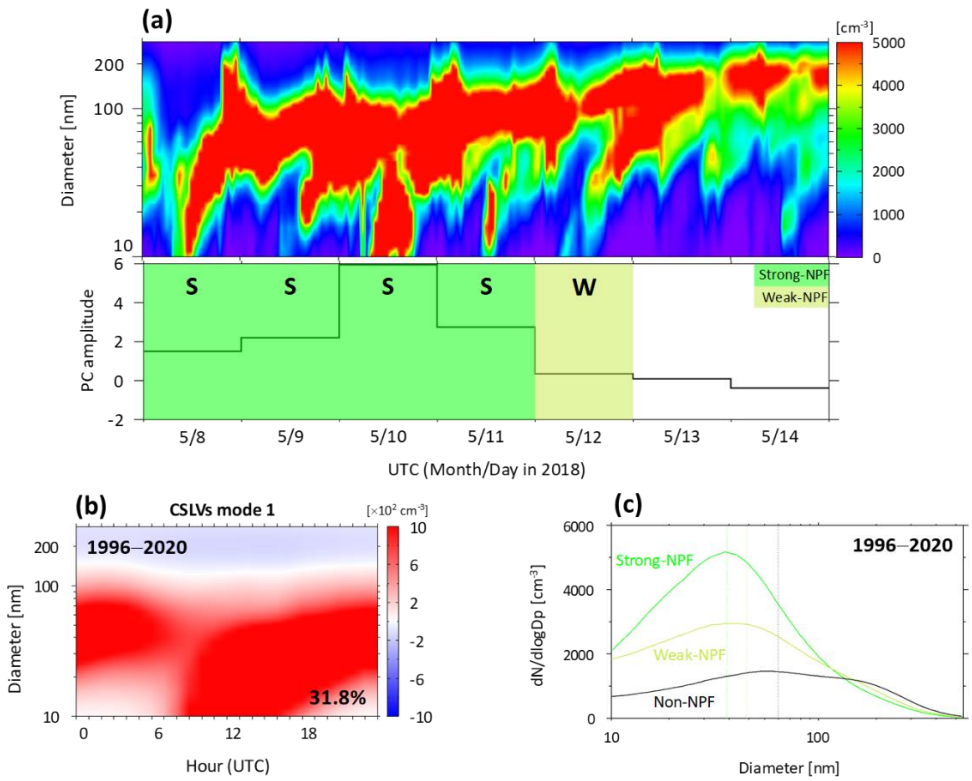

Figure 4.2. An example of NPF identification using observed PNSD in HYY during 8–14 May, 2018. (a) Observed PNSD during 8–14 May, 2018 (upper), and corresponding PC amplitude and classification result (lower). (b) CSLV for the PNSD measured from 1996 to 2020. (c) PNSD during strong- (green), weak- (yellow), and non-NPF events (black).

A yearly variation of NPF frequency estimated by CSEOF technique is represented on **Figure 4.3**. Although non-NPF frequency was highest, NPF frequency was about 40% before 2008 and it has reduced to about 30% recently. As a result, trend estimated based on the linear regression line was about -0.58% yr^{-1} and -0.27% yr^{-1} for entire NPF (strong- and weak-NPF) and strong-NPF, respectively. This example suggested that HYY station experienced not only a decadal decrease of entire NPF frequency, but also the decadal decrease of the occurrence of a clear NPF until a recent date.

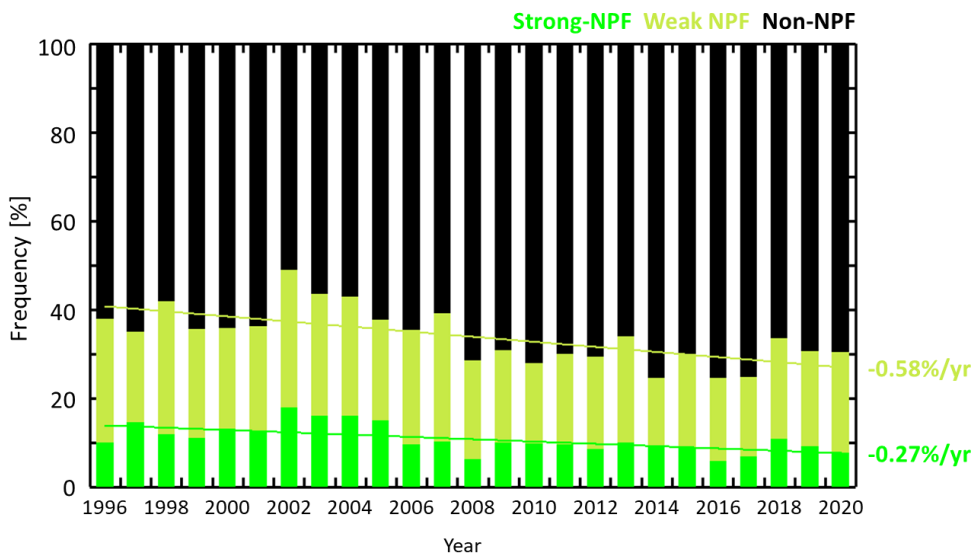

Figure 4.3. Yearly variation of frequency of strong- (green), weak- (yellow), and non-NPF events (black) in HYY from 1996 to 2020.

NPF frequencies estimated in 27 selected lowland sites based on the CSEOF technique were organized in **Figure 4.4**. NPF frequency was highest in urban regions, accounting for around 43% of total days. NPF frequency estimated in urban stations was about 6% higher than entire median NPF frequency. For previously stated roadside stations, NPF occurrence was more frequent in roadside stations (DRN) than DRW, while it was opposite for LEI stations (NPF occurrence in LEI-E was rarer than LEI-M), possibly causing relatively low in N_{tot} in LEI-E. As for other environments, the relatively low NPF frequencies were generally estimated at the observation environments whose anthropogenic influences are minimal. Many previous literatures explain NPF occurrence in terms of the low-volatile precursor vapors (ex. Zhao et al., 2015), but several works reported that NPF occurrence under low CS despite of high precursor vapor concentration (ex. Dai et al., 2017). The NPF frequency estimated in this study implies that environmental difference in the precursor emissions can be a more crucial factor in NPF occurrence than that in the CS in the competitive relationship between precursor emissions and condensation or coagulation sink built by pre-existing large particles in the ambient atmosphere.

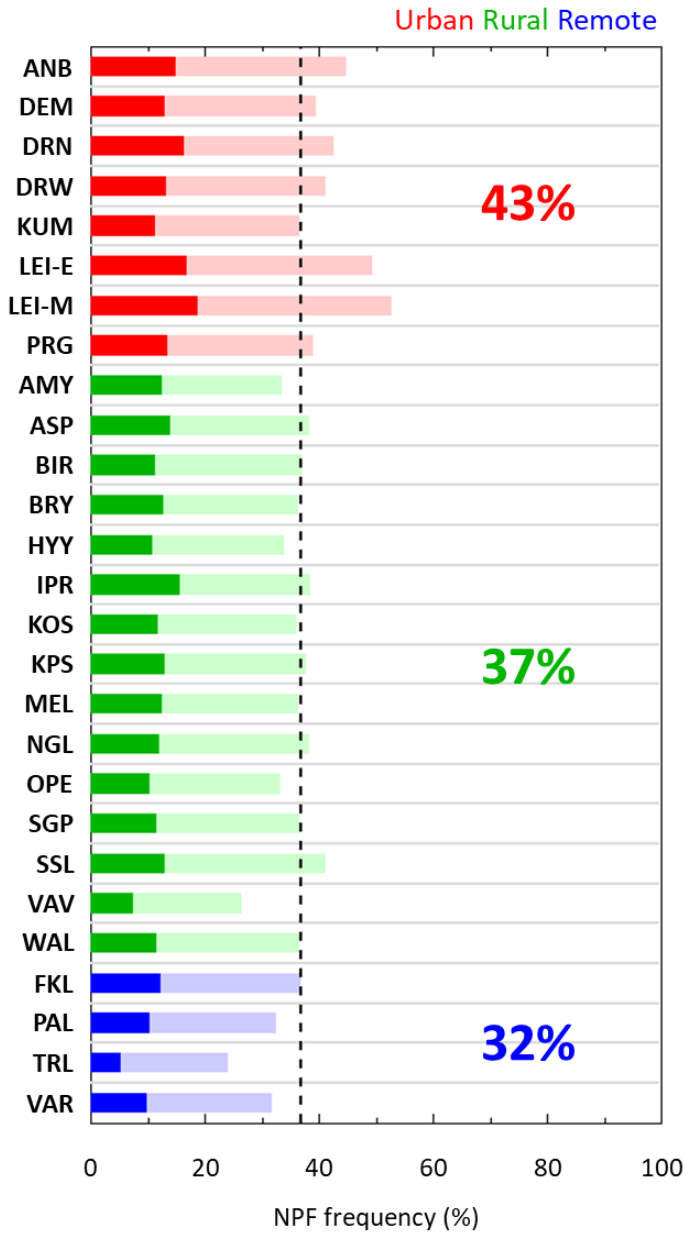

Figure 4.4. NPF frequencies estimated in 27 selected lowland sites based on the CSEOF technique. Strong-NPF frequencies are marked as red/green/blue for urban/rural/remote sites, respectively, and weak-NPF frequencies are marked as more light color. Black dashed line is an entire median of NPF frequency for all the observation environments.

NPF intensity such as 10-nm particle FR (cm^{-3} s^{-1}) and GR (nm h^{-1}) was also characterized (**Fig. 4.5**). The FR was calculated using the equation represented in Dal Maso et al. (2005). Because there are few particles growing more than 20–30 nm before the formation completed, the upper limit of nucleation-mode size range was set as 25 nm to neglect the flux of particles escaping from the size range (Dal Maso et al., 2005; Kerminen et al., 2018). The GR was estimated by tracking the change of mode diameter according to time using linear fit (Lehtinen and Kulmala, 2003). 10-nm particle FR and GR showed moderate positive correlation because condensing vapors (e.g. H_2SO_4) participating in the particle formation are also partially associated with particle growth. FR had larger environmental variability than GR, showing around 1.78±1.53 cm^{-3} s^{-1} in urban and 0.20±0.57 cm^{-3} s^{-1} in remote sites, resulting in urban FR showing around 1 order higher value than remote site. However, environmental difference in GR was relatively smaller, showing only slight difference between urban GR (4.20±3.62 nm h^{-1}) and remote GR (3.31±2.84 nm h^{-1}). Relatively low environmental variability of GR can be explained by substantial participation of oxidants of biogenic precursors (e.g. monoterpene or isoprene) in growth processes at rural and remote sites (Petäjä et al., 2022).

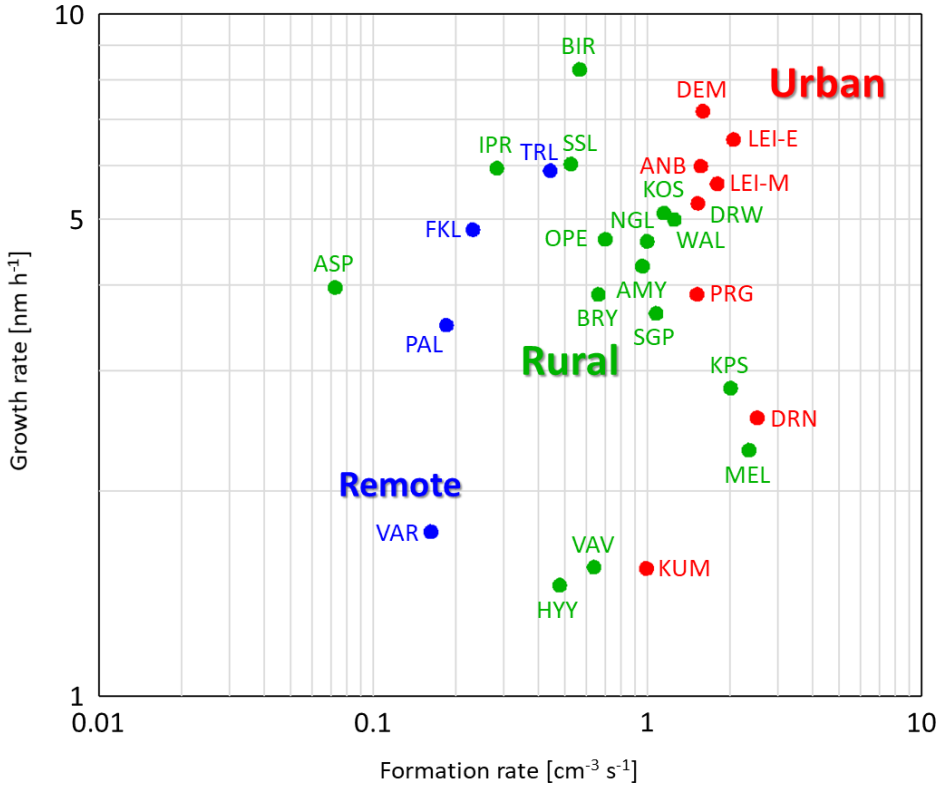

Figure 4.5. Averaged FR (10 nm) and GR for all available data measured in each measurement sites.

For systematic PNSD analysis, PNSD was divided into three groups: particle number concentration of total- (10–500 nm; N_{tot}), nucleation- (10–25 nm; N_{nuc}), and accumulation (100–500 nm; N_{acc}) modes. **Figure 4.6** displays all-time averaged N_{nuc} ratio [$N_{nuc}/(N_{nuc}+N_{acc})$] according to increasing N_{tot} derived based on the all available data in each station. Overall, N_{tot} level is several thousands of cm^{-3} in urban and rural sites, but showed only several hundreds of cm^{-3} in remote sites except for FKL.

Generally, N_{nuc} ratio is higher in the region close to anthropogenic sources, showing significant site-to-site variations. Taken together with the description associated with N_{tot} in **Table 4.1** and the ranking of N_{tot} in **Figure 4.6**, N_{nuc} can dominantly contribute in determining N_{tot} in urban regions. In other words, the frequency or intensity of NPF is important for explaining N_{tot} in the regions close to the anthropogenic emission sources. Meanwhile, Rural regions where the influence from local emissions also exist (ex. IPR) show N_{tot} comparable to that estimated in urban regions (Gilardoni et al., 2011), despite low N_{nuc} ratio. Furthermore, remote sites have most variable N_{nuc} ratio, representing extremely low N_{nuc} ratio in FKL (~15%) or high N_{nuc} ratio in TRL (~75%). Especially, unlike other remote stations, observed PNSD in TRL generally showed unimodal shape regardless of the season. Burst of the number concentration in a lower diameter mode in local spring/summer under relatively low number in higher diameter mode was regarded to lead the sharp increase on N_{nuc} ratio in TRL (Rose et al., 2021).

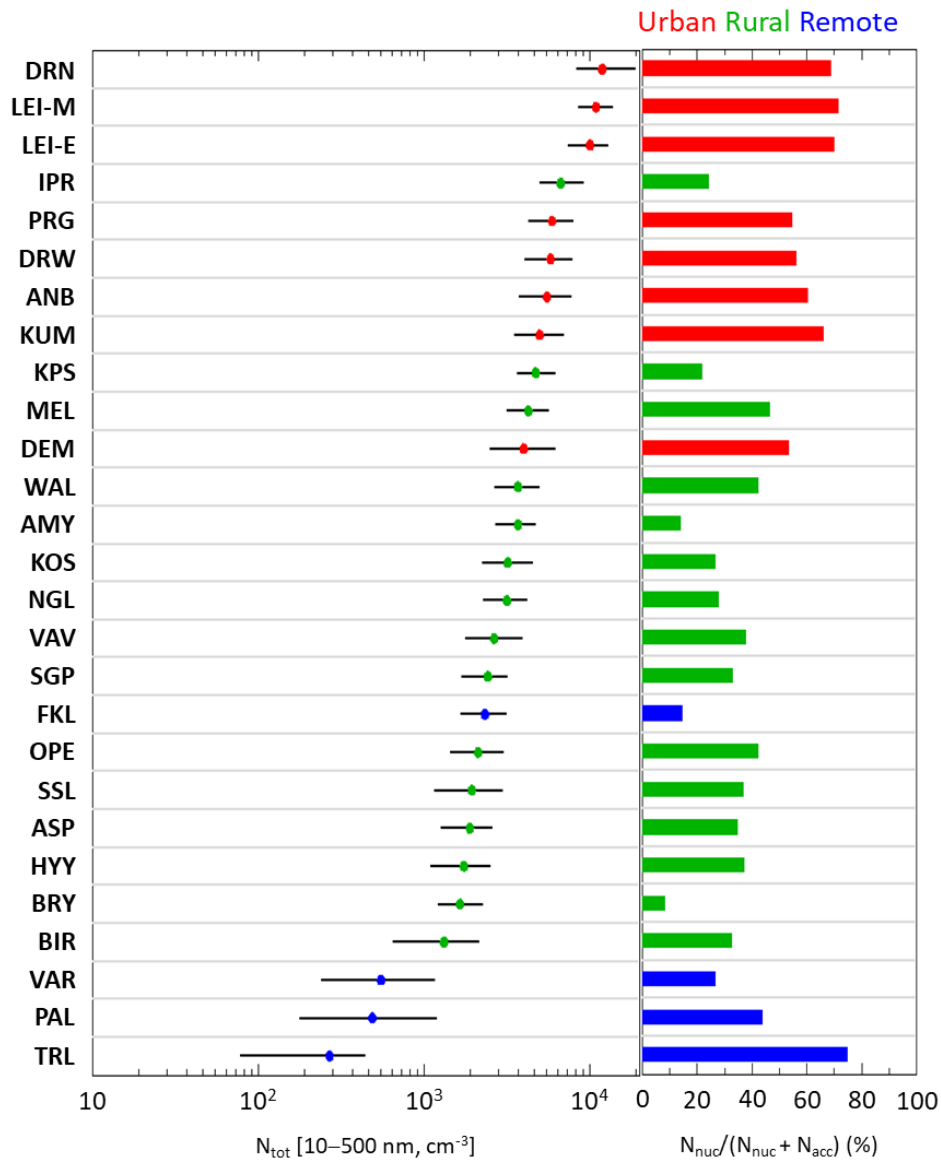

Figure 4.6. N_{tot} arranged with the value (Left) and N_{nuc} ratio ($N_{nuc}/(N_{nuc}+N_{acc})$) according to N_{tot} (Right). On the left figure, 1st and 3rd quartile of N_{tot} are represented as bar graph. Dot in the left figure and bar in the right figures are represented as color symbolizing each environment (red: urban, green: rural, and blue: remote).

Overall environmental characteristics of PNSD is represented on **Figure 4.7**. Basically, $dN/dlogD_p$ of almost all the diameter range was highest in urban regions, showing a peak around 9000 cm^{-3}. PNSD observed at all the environment showed unimodal shape, while the location of uni-modal peak was lowest (~19 nm) in urban environment. Because nucleation-mode particles can be emitted by vehicular exhaust but largely produced by NPF and subsequent growth (Rose et al., 2021), shift of peak location to the lower diameter in urban environment is attributable to the frequent or intense NPF. PNSDs derived from rural and remote sites had a similar peak diameter (~58 nm for rural and ~56 nm for remote sites) under enhanced influence of more aged particles.

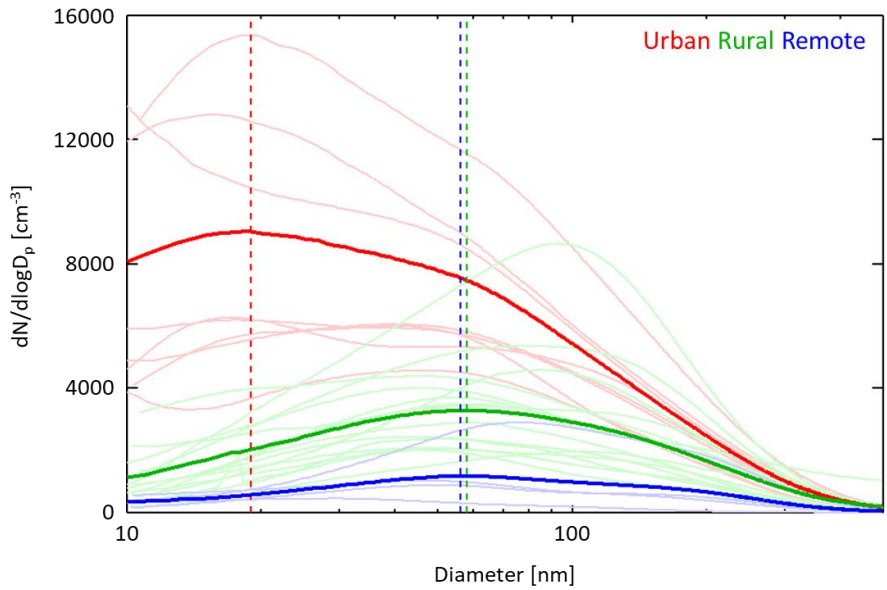

Figure 4.7. PNSD for each environment. Lines with each light color represent the all-period average of PNSD for each sites, and lines with dark color display the average of all stations in each environment (red: urban, green: rural, and blue: remote).

Overall environmental characteristics in relationship between N_{tot} and N_{nuc} or N_{acc} are displayed on **Figure 4.8**. **Figure 4.8** shows the ratio of N_{nuc} or N_{acc} to N_{tot}, respectively, for all available data for each observation environment. Differing from N_{acc}, N_{nuc} shows large site-to-site or temporal variability in rural and remote regions, resulting in the calculated N_{nuc} ratio are located in a wider range of N_{nuc} ratio from 1:1 to 1000:1 line, than N_{acc} ratio. The highest correlation between N_{nuc} and N_{tot} in urban regions (r=0.88) implied the systematic and significant contribution of N_{nuc} to N_{tot}. Especially, only correlation of N_{nuc} with N_{tot} in

urban regions was higher than that of N_{acc}, implying the close connection between newly-formed particles originated from frequent/intense NPF and total aerosol number concentration. Compared to the correlation of urban regions, those estimated in the rural and remote regions were relatively low and similar to each other (r=0.60 in rural and r=0.55 in remote sites) due to the large variability of N_{nuc} according to the occurrence of NPF. This implied that N_{tot} are largely dominated by N_{nuc} primarily produced from frequent/intense NPF and subsequent growth, which is consistent with the results represented on **Figure 4.8**.

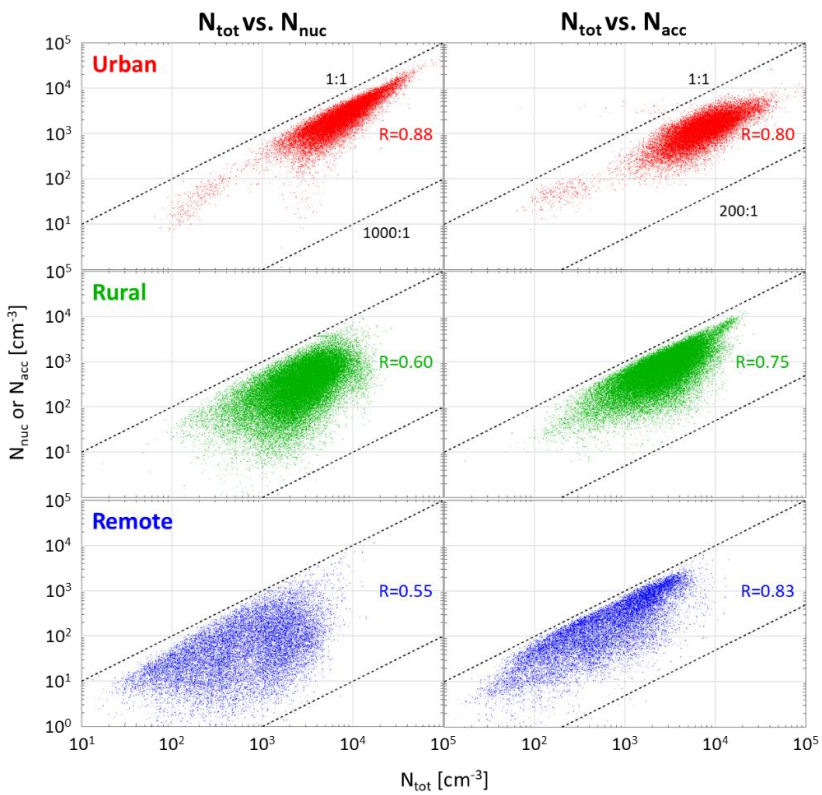

Figure 4.8. Scatter plot representing ratio of N_{nuc} (left), and N_{acc} (right) to N_{tot} in urban (red), rural (green), and remote (blue).

4.2 Global trend of PNSD and NPF

Based on all available data summarized in **Table 4.1**, global trend of PNSD, especially N_{nuc} which is a parameter directly associated with NPF, and NPF frequency could be basically estimated by linear regression. In addition, Mann-Kendall (MK) trend test would be applied to the yearly time series of N_{nuc} or NPF frequency. In the MK test, Kendall statistics S is defined by the sum of all possible difference among the elements in the time series. Based on the variance of S originated from the number of data, Z statistics is calculated using S as well as variance of S. By finding p-value corresponding to Z statistics, statistically significant monotonic increasing or decreasing trend can be detected at the 90% confidence level. In this study, MK test was conducted for the time series longer than 8 years because slope and confidence limits for the aerosol optical properties was reported to be significantly unstable for the time series shorter than 8 years according to Collaud Coen et al. (2020). When MK test result is represented, Sen's slope was expressed together based on the median of the slopes derived by all available data pairs. By utilizing Sen's slope, expressed decadal trend can be less affected by unexpected extreme value.

Decadal trends of N_{nuc} expressed by linear regression and Sen's slope were displayed in **Figure 4.9**. The magnitude and directionality of trends from linear regression were generally similar to those estimated

from Sen's slope. Most of the urban regions experienced a decadal decrease of N_{nuc}, except for LEI-M. Especially, ANB, DRN, DRW, and KUM showed statistically significant decrease in N_{nuc}. Considering DRN and LEI-E are roadside stations, impacts from vehicular exhaust on N_{nuc} were regarded to decrease in urban regions. Meanwhile, stations in LEI showed opposite direction between each other in the N_{nuc} trend. These negative decadal N_{nuc} trend was also for most of the rural regions, but BIR and OPE exhibited statistically significant positive trends in N_{nuc}.

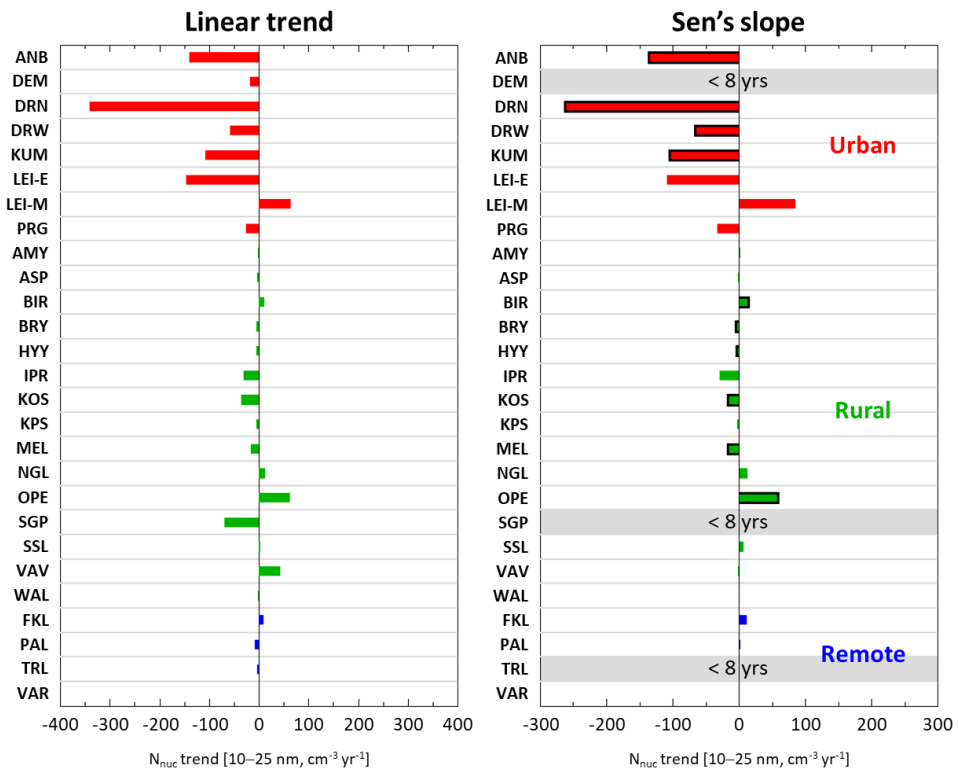

Figure 4.9. Decadal trends of N_{nuc} estimated from linear regression (left) and Sen's slope (right). Solid lines were added to the statistically significant trend identified by MK test.

Nocturnal N_{nuc} trend was further analyzed by decomposing trend into daytime and nighttime (**Fig. 4.10**). After calculating local time of sunrise and sunset based on the geographical location (latitude & longitude) of the stations, daytime (nighttime, in parenthesis) was set as the local time between an hour after sunrise (sunset) and an hour before sunset (sunrise). Generally, all the sites had a consistent N_{nuc} trend between daytime and nighttime, even in the stations with positive N_{nuc} trend (e.g. BIR, OPE) in the aspect of the statistically significant overall N_{nuc} trend. For statistically significant negative N_{nuc} trend mainly concentrated on the urban sites (ANB, DRN, DRW, and KUM), decadal decrease of daytime N_{nuc} was sharper than that during the nighttime. Daytime N_{nuc} trend in urban regions ranged from about -400 cm^{-3} yr^{-1} in DRN to -100 cm^{-3} yr^{-1} in DRW, but the influence of decadal daytime decrease of N_{nuc} closely connected with daytime NPF occurrence remained until nighttime in a measure, resulting in a N_{nuc} trend in a range from -200 cm^{-3} yr^{-1} in DRN to -50 cm^{-3} yr^{-1} in DRW.

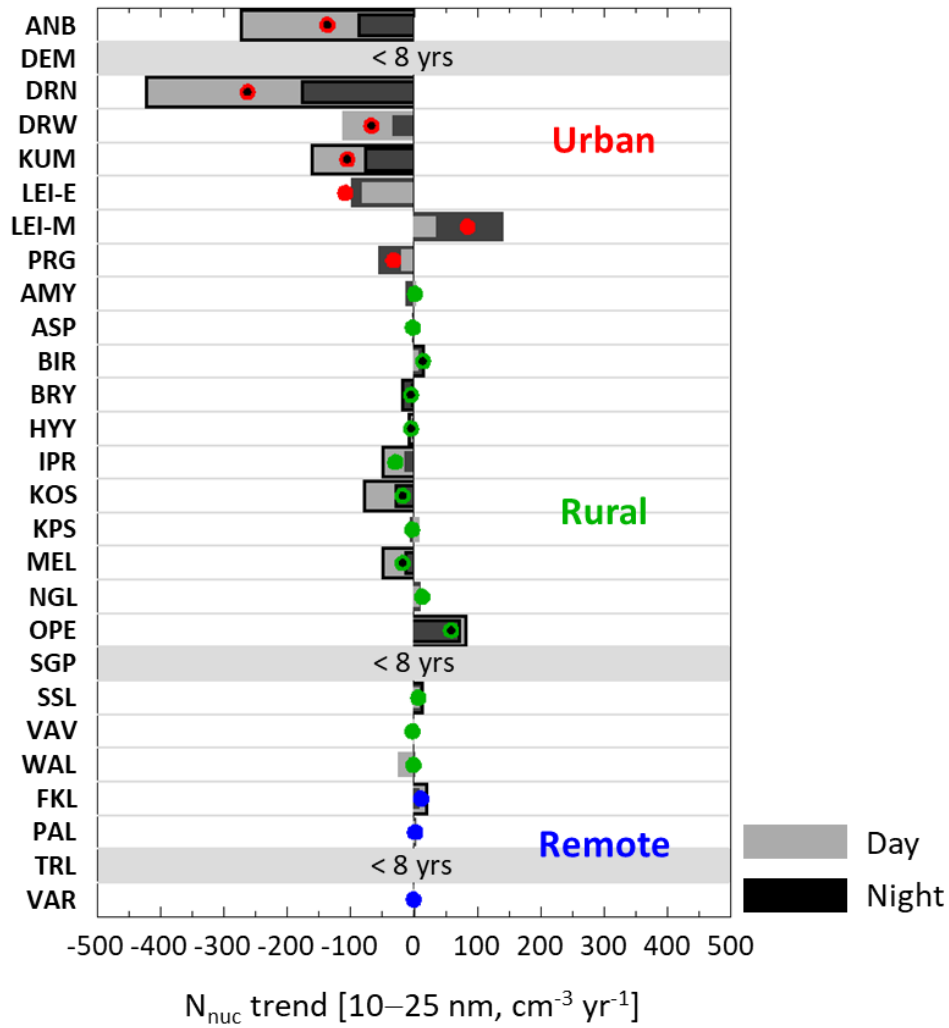

Figure 4.10. Decadal trends of N_{nuc} estimated during local daytime (gray) and nighttime (black). Overall N_{nuc} trend is represented as color dot and black dot was further added for the statistically significant N_{nuc} trend.

NPF frequency trends estimated in 27 selected lowland sites using CSEOF technique were represented on **Figure 4.11**. As for the linear trend, most of the urban regions showed negative trend in both strong and entire NPF frequency, except for the entire NPF frequency in DEM.

There are complex decadal changes in NPF frequencies in rural regions according to the favorable conditions for the transport of air pollutants. However, all statistically significant Sen's slopes were negative regardless of observation environmental types or clearness of NPF occurrence. Among the observation environments, urban sites experienced most drastic decrease of NPF frequency from about -3.5% yr^{-1} in KUM to -4.2% yr^{-1} in DRN. Although there was no statistically significant trend both in N_{nuc} and NPF frequency in remote sites, many of the rural sites showed significant decadal decrease of N_{nuc} and it was closely associated with the clear decrease of NPF occurrence of about 0.5–1.0% yr^{1} in HYY and MEL. Site-to-site demonstration of NPF frequency change is beyond the scope of this study, but rural sites showing significant decadal decrease can be under the favorable conditions for the transport of decreased air pollutants from upwind anthropogenic source region (e.g. BRY). Documented NPF frequency trend in this study was consistent to the previous studies for urban (Saha et al., 2018; Pittsburgh), rural (Wang et al., 2017; MEL), and remote sites (Asmi et al., 2011; PAL).

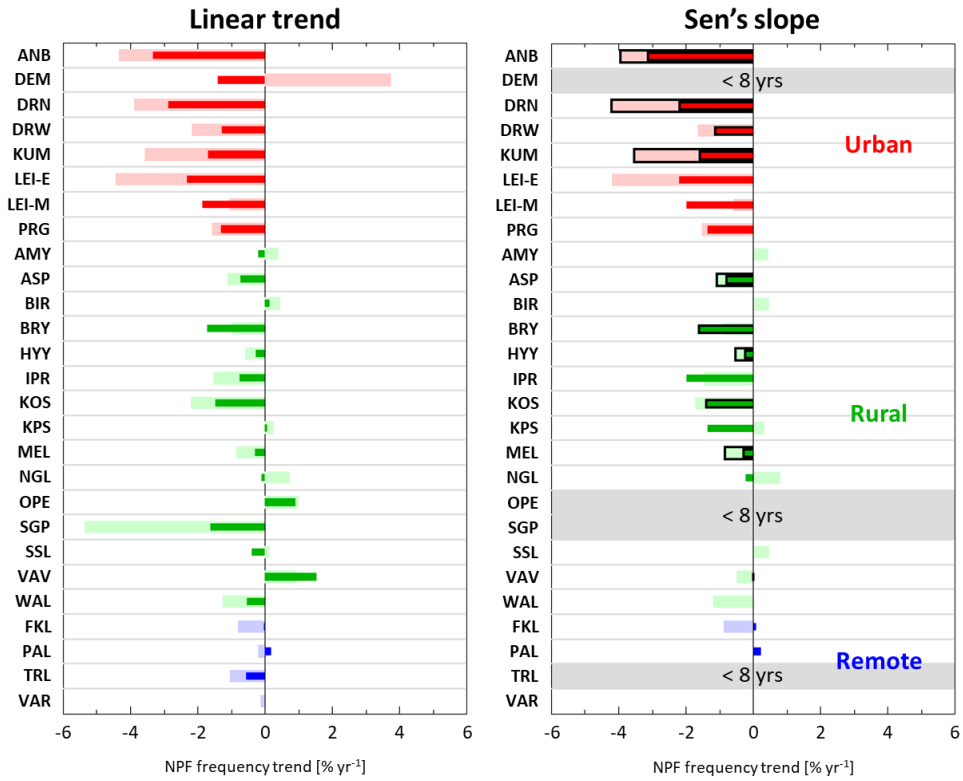

Figure 4.11. Decadal trends of NPF frequency estimated from linear regression (left) and Sen's slope (right) for strong-NPF (thin bar) and entire (strong- and weak-) NPF (thick bar). Solid lines were added to the statistically significant trend identified by MK test.

Summarized figure for NPF frequency, its trend, and N_{nuc} trend are presented as **Figure 4.12**. Generally, directions of NPF frequency trends were generally consistent with those of N_{nuc} trend in most of the stations. Considering only statistically significant positive trend was estimated at BIR in terms of N_{nuc}, most of the negative NPF frequency trends were closely connected with the negative N_{nuc} trends in most of the stations regardless of the observation environmental types. However, it was not the case in several stations such as LEI-M. Trend of NPF frequency in LEI-M was completely opposite to that of N_{nuc}, implying other emission sources have been contributed to direct emission of N_{nuc} by combustion processes possibly related to industrial field or residential heating. As stated above, impacts of consistent and intense global regulations for the atmospheric precursors (e.g. SO_2) on the NPF occurrence are an interesting subject to study because their influences on NPF occurrence are currently controversial, contrary to relatively well documented connection between the concentration of H_2SO_4 and particle formation rate. From the report of this study, significant contribution of reduced gaseous precursor emissions to the suppression of NPF occurrence was identified using available global cutting-edge *in-situ* observations.

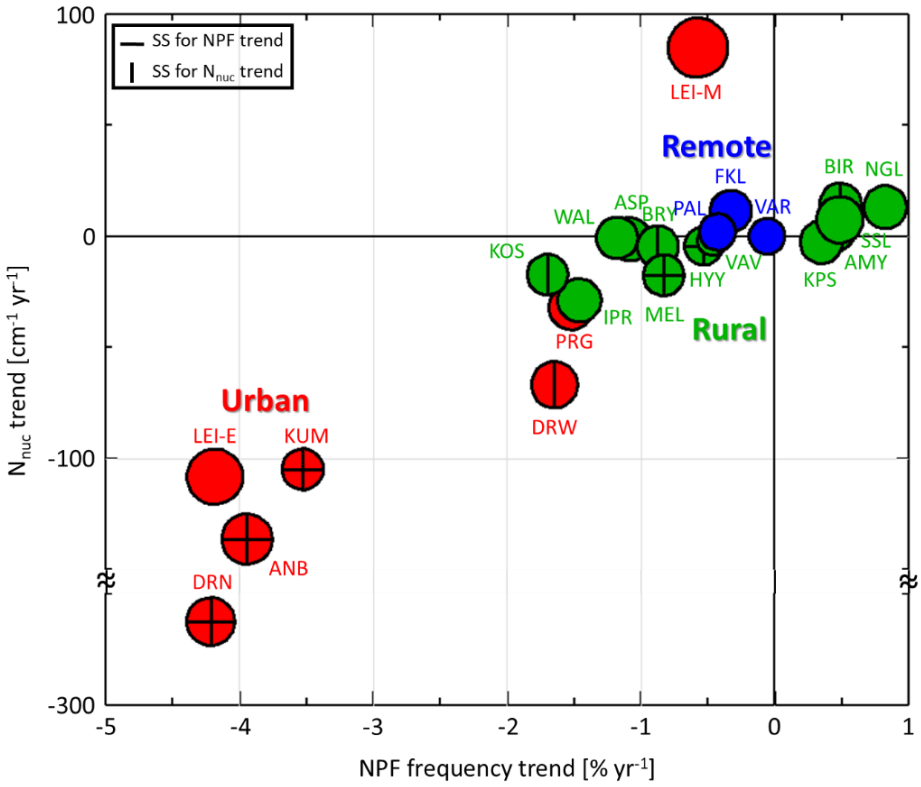

Figure 4.12. Scatter plot between NPF frequency trend and N_{nuc} trend for urban (red), rural (green), and remote (blue) sites. Horizontal and vertical lines are added to the symbol if NPF frequency trend and N_{nuc} trend are statistically significant (ss) at 90% significance level, respectively. The size of the symbols reflects the NPF frequency of each sites.

4.3 Influence of the global NPF change on the CCN-sized aerosols

If freshly formed particles can successfully grow until the CCN-size, they can act as CCN. In addition to the literatures introduced in the section 1, NPF events accompanied by subsequent growth as a significant contributor to CCN budget are analyzed using long-term observations more than a year. When NPF occurs, CCN concentrations was increased by a few hundred percent at the European sites in the continental BL (Kerminen et al., 2012). Furthermore, it can be speculated that the relative CCN concentration increase in the FT can be more severe (~500%) than that in the BL based on the annual observation conducted in the FT over summit of Mount Chacaltaya (Rose et al., 2017).

Despite the importance of NPF in terms of producing CCN, the spatial coverage of CCN observation is limited. Among the stations enrolled in GAW World Data Centre on Aerosols (WDCA), only four European stations (Hyytiälä, Jungfraujoch, Vavihill, Mt. Zeppeline) and an Australian site (Cape Grim) are operating CCN counter (CCNC). Under this circumstance, some model studies yielded meaningful estimation of the impact of NPF on the global CCN. Using aerosol microphysics model, Spracklen et al. (2008) concluded that global mean CCN concentrations under 0.2% supersaturation increased by 3–20% due to particle formation during the springtime. Meanwhile, Merikanto et al. (2009)

estimated that about 45% of the global low-level cloud CCN at 0.2% supersaturation was secondary aerosols formed by nucleation.

To imbue a meaning in terms of climate to the analyzed trend of NPF frequency, it is necessary for the connection between the change of NPF and CCN budget. In this study, observation-based examination of the relationship between decadal global NPF change and potential CCN was conducted using a simpler approach adopted by many previous works (Jurányi et al., 2011; Kerminen et al., 2012; Hoyle et al., 2016; Rose et al., 2017; 2019). Although all the particle grown to CCN-size cannot act as a CCN, CCN-sized aerosols can be regarded as potential CCN. For example, Hoyle et al. (2016) reported that 79% of observed variance of cloud droplet number in Jungfraujoch station was explained through CCN number concentration by assuming particles larger than 80 nm as a potential CCN.

Though many literatures conducted meaningful validation of the assumption regarding CCN-sized aerosols as potential CCN, this study investigated the relationship between the number concentration of CCN-sized aerosols and CCN itself using all available simultaneous in-situ observation using MPSS and CCN counter in HYY and VAV before adopting the assumption. **Figure 4.13** and **4.14** shows the relationship between CCN concentration and CCN-sized aerosols estimated by three

different size-cut (50, 80, and 100-nm) under different supersaturation ratios in HYT and VAV, respectively. The number concentration of CCN-sized aerosols was generally well matched with the CCN number concentrations at the most of supersaturation level. Among CCN-sized aerosols, correlation between CCN number concentration and N_{50} (Number concentration of aerosols larger than 50 nm) increased with the supersaturation ratio in both HYY and VAV, but correlations of N_{80} or N_{100} were highest at intermediate supersaturation level. Especially, correlation was relatively high at representative supersaturation range of ambient atmosphere (0.3%–0.5%; Jung et al., 2018) regardless of size cuts of CCN-sized aerosols. For HYY, correlation of N_{80} (r=0.86) and N_{100} (r=0.86) was higher than that of N_{50} (r=0.76) at supersaturation of 0.3%, but correlation of N_{50} became significantly better (r=0.83) at supersaturation of 0.5%. For VAV, correlation of N_{50} (r=0.77) and N_{80} (r=0.77) was distinctly higher than that of N_{100} (r=0.72) at supersaturation of 0.4%. Aforementioned literatures adopted diverse size-cuts for regarding CCN-sized aerosols as potential CCN because activation diameter of CCN-sized aerosols can be changed according to the supersaturation ratio of atmosphere (Hammer et al., 2014; Motos et al., 2019). For example, Hoyle et al. (2016) examined the relationship between CCN number concentration and CCN-sized aerosols estimated from the size-cut from 70 nm to 100 nm. In addition, Rose et al. (2017)

analyzed the increase of the CCN-sized aerosols from NPF events in the free troposphere by examining the change of N_{50}, N_{80}, and N_{100}. This approach became a basis for the global study of the fraction of CCN-sized aerosols among the total PNSD, which regarded the CCN-sized aerosols as N_{50} or N_{100} in Rose et al. (2021). Observation-based analysis of CCN-sized aerosols with NPF origin can be more difficult with the increase of the size-cut of CCN-size due to the direct emission of accumulation-mode particles, although the analysis is conducted only for the NPF events. In this study, N_{50} was adopted for the representative of potential CCN.

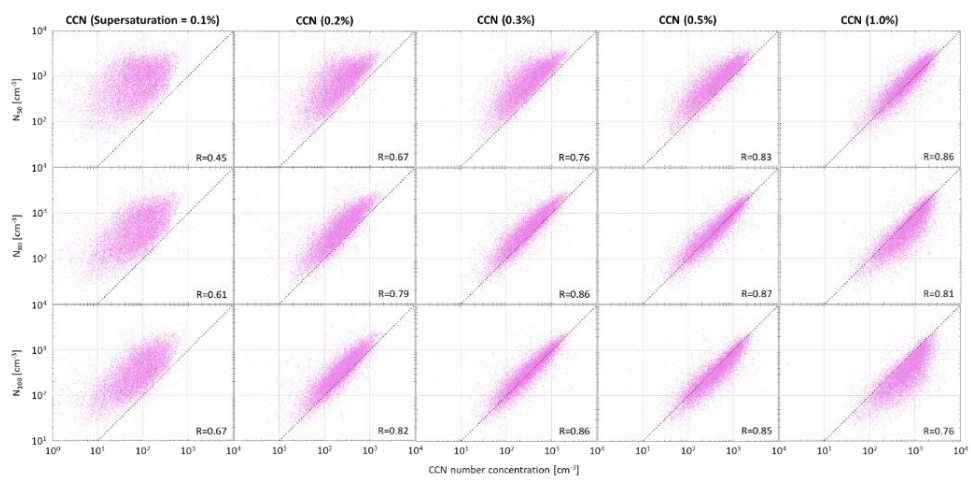

Figure 4.13. Scatter plot for CCN number concentration at different supersaturation (SS) level (0.1%, 0.2%, 0.3%, 0.5%, and 1.0%) versus CCN-sized aerosols (N_{50}, N_{80}, and N_{100}) observed during the period of 2013–2020 in HYY station. Correlation coefficients are written at the lower right of each plot.

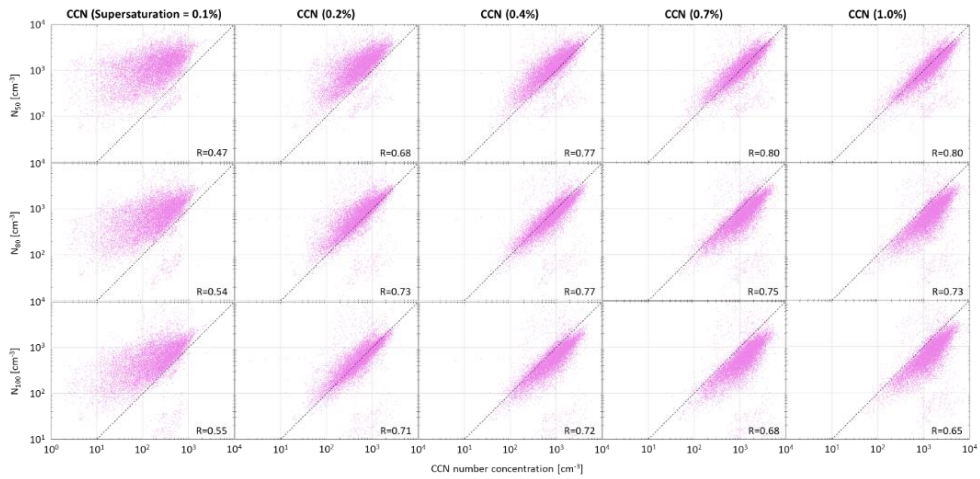

Figure 4.14. Scatter plot for CCN number concentration at different supersaturation level (0.1%, 0.2%, 0.4%, 0.7%, and 1.0%) versus CCN-sized aerosols (N_{50}, N_{80}, and N_{100}) observed during the period of 2008–2016 in VAV station. Correlation coefficients are written at the lower right of each plot.

Number concentration of CCN-sized aerosols (N_{50}) during non-NPF and NPF events is presented on **Figure 4.15**. N_{50} during NPF events was significantly higher than that during non-NPF events, showing 76%, 72%, and 170% higher concentration in urban, rural, and remote sites, respectively. Because overall N_{50} during non-NPF was lowest in remote sites (~400 cm^{-3}), proportional increase of the N_{50} during NPF events was relatively higher than that of other environments, which was consistent to the largest increase N_{50} via NPF estimated in PAL in Kerminen et al. (2012). However, magnitude of proportional increase of N_{50} was lower than estimation for rural and remote sites in Kerminen et

al. (2012) possibly because only type I NPF (Dal Maso et al., 2005) was considered to estimate the impact of NPF on CCN concentration. For urban regions, proportional increase of N_{50} via NPF events was even higher than that of rural stations despite the overall high N_{50} level in urban sites under relatively high GR of urban NPF events. Direct measurement of CCN number concentration in urban background site (de España et al., 2017) showed rather weaker increase of CCN number concentration from the occurrence of NPF events than estimation in urban sites of this study. This analysis suggested that NPF events can contribute to the budget of relatively larger particles that can act as CCN as well as nucleation-mode particles.

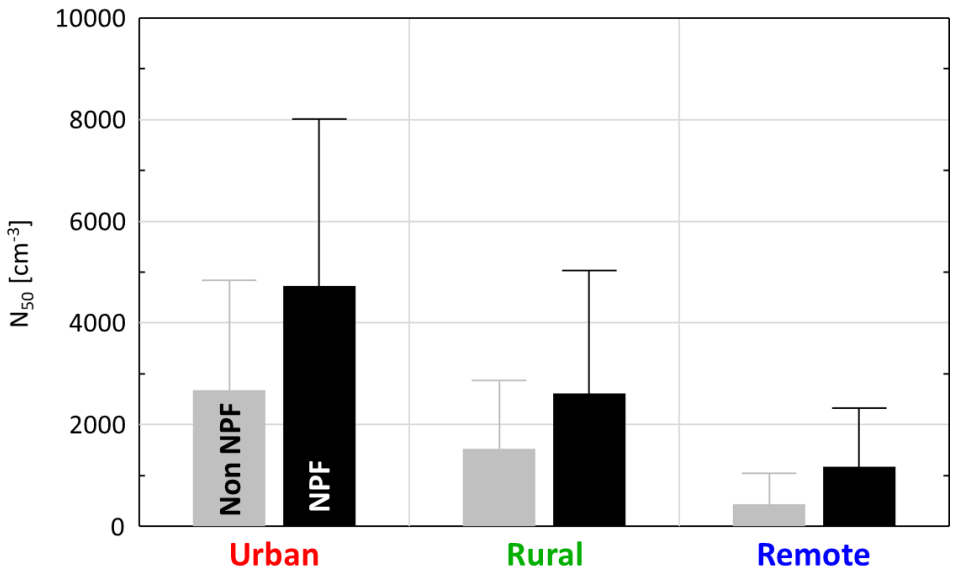

Figure 4.15. Overall mean and standard deviation of N_{50} during non-NPF and NPF in urban, rural, and remote environments.

The relationship between NPF frequency trend and N_{50} trend was summarized on the scatter plot of **Figure 4.16**. Although the occurrence of NPF might not be directly related to N_{50}, all of the statistically significant trend was negative in both of NPF frequency and N_{50} trend regardless of the observation environments. Decadal decrease of N_{50} was the most distinct in urban regions in which KUM (~ -120 cm^{-3} yr^{-1}), ANB (~ -190 cm^{-3} yr^{-1}), and DRN (~ -320 cm^{-3} yr^{-1}) especially showed obvious negative N_{50} trend closely connected with the decadal decrease of NPF occurrence. This significant negative trends of N_{50} were also captured in many of the rural sites. Among them, ASP, MEL, and HYY showed significant decrease of NPF frequency as well as N_{50}, although the magnitude of N_{50} decreases were lower than 50 cm^{-3} yr^{-1}. Meanwhile, meaningful negative trend of N_{50} even existed in remote sites (VAR), showing about -7 cm^{-3} yr^{-1}. This global decadal decrease of potential CCN closely connected with declined NPF occurrence can possibly have a huge impact on the aerosol indirect effect in atmospheric clouds.

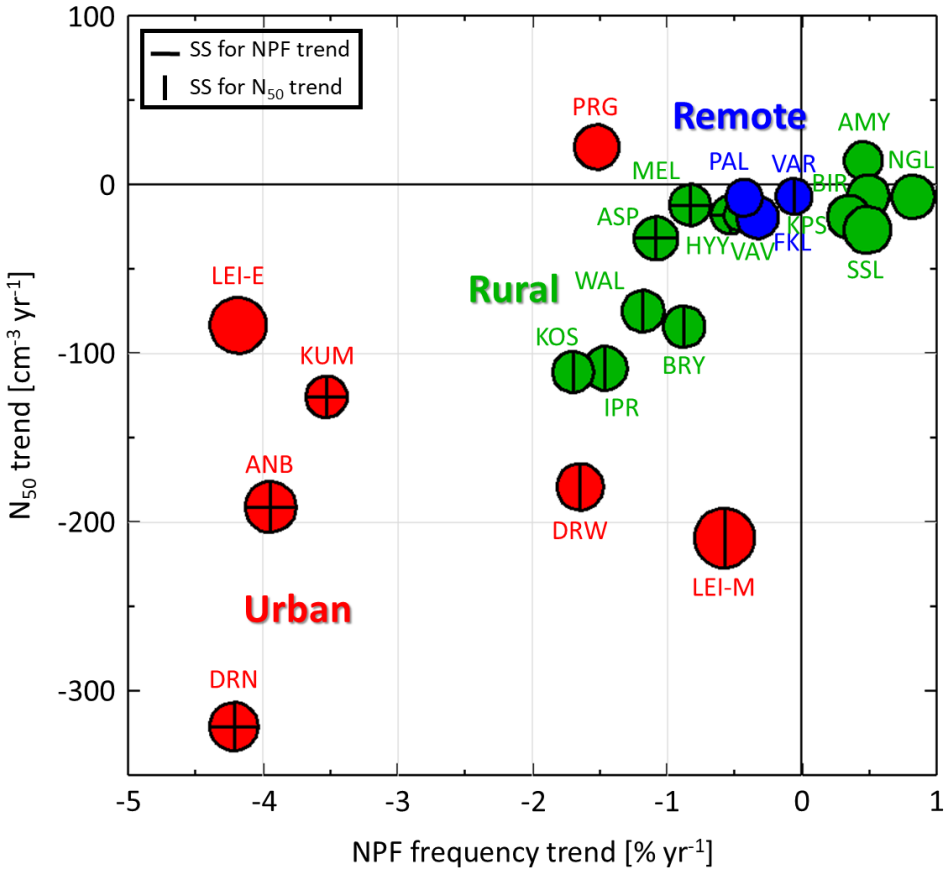

Figure 4.16. Scatter plot between NPF frequency trend and N_{50} trend for urban (red), rural (green), and remote (blue) sites. Horizontal and vertical lines are added to the symbol if NPF frequency trend and N_{50} trend are statistically significant (ss) at 90% significance level, respectively. The size of the symbols reflects the NPF frequency of each sites.

Chapter 5. Summary and conclusions

To understand the spatial characteristics of PNSD and NPF over Korean Peninsula, a case analysis was conducted for NPF cases in the FT during KORUS-AQ campaign by taking advantage of the DC-8 aircraft observations. SO_2-to-sulfate conversion seemed to highly influence the FT NPF event over YS. Gas-phase and aqueous-phase pathways were thought to be participated in the sulfate formation, as indicated by positive correlation of sulfate-to-CO ratio with both temperature and RH. The production of high level of SO_2 by the transport from upwind regions above the shallow marine boundary layer might be attributed to the sulfate formation under the favorable conditions for the NPF in the FT. It was identified that $N_{CN3\text{-}10}$ generally decreased with increasing altitudes, reaching 7606±12003 cm^{-3} in the daytime BL. In addition, the number density of particles with diameters from 10 nm to 15 nm was higher than ~10000 cm^{-3} near the surface. Vertical distribution of nucleation-mode particles indicated that NPF occurrence around the Korean Peninsula during the KORUS-AQ campaign was the most frequent or intense in the BL.

Evaluation related to the impact of the change in condensing vapors on the PNSD and NPF over Asian continental outflow was conducted by

analyzing the impact of the COVID-19 LD in the upwind regions on the NPF frequency and corresponding PNSD at three regional background sites located west of the Korean Peninsula. Although the number concentrations of nucleation- and accumulation-mode particles decreased during the LD period (February to March 2020) in BRY, the PNSD of AMY showed only a slight decrease of particle number concentrations in nucleation- and accumulation-mode under the impact of local emissions. The BOS experienced similar variations in the PNSD to those of BRY; however, the magnitude was smaller, showing a decrease of 11% in the nucleation-mode and 24% in the accumulation-mode.

The CSEOF technique-based classification of NPF events showed that NPF frequency decreased at all sites, despite the generally more favorable meteorological conditions for the occurrence of NPF during the LD period. Considering the substantial contribution of inorganic components to the particulate matter in East Asia, the diurnal variation of sulfuric acid (H_2SO_4) proxy was investigated to analyze the occurrence of NPF events. The H_2SO_4 proxy during 8–12 LST was a significant factor for the occurrence of NPF in AMY and BOS during both the Pre-LD (February to March of 2013–2019) and LD periods; however, the difference between NPF and non-NPF events was not statistically significant in BRY. BRY showed the highest H_2SO_4 proxy relative to CS ([H_2SO_4 proxy]/[CS]) compared to the other sites, implying that the

H_2SO_4 proxy could be saturated for limiting NPF occurrence. The less frequent outbreak of NPF events in BRY during the LD period can be attributed to the influence of the reduced emission of organic vapors from the Asian continent. This is because BRY is more susceptible to emission changes from hotspot regions than other sites are.

In terms of expansion of spatio-temporal scale, environmental elaboration of PNSD and NPF was conducted based on the decadal-scale multi-year measurement. Taking advantage of SARGAN, 27 lowland sites (8 urban, 15 rural, and 4 remote sites) were selected to understand global PNSD and NPF.

CSEOF-based identification of NPF days was also conducted for global PNSD to estimate NPF frequency. NPF frequency was highest in urban regions, occurring around 43% of total days. Also, the relatively low NPF frequencies were generally estimated at the observation environments whose anthropogenic influences are minimal. Based on the documented NPF frequency, the magnitude of precursor emissions can be a more important factor in NPF occurrence in the competitive relationship between precursor emissions and condensation or coagulation sink built by pre-existing large particles in the ambient air. Under the participation of several condensing vapors in formation as well as growth (e.g. H_2SO_4), 10-nm FR showed moderate positive correlation with GR. FR had larger environmental variability than GR, while

environmental difference of GR was less than that of FR due to substantial participation of low-volatile oxidants of biogenic precursors.

PNSD observed at all the environment showed unimodal shape. Generally, $dN/dlogD_p$ was the highest in urban, followed by rural and remote regions. The location of uni-modal peak was the lowest in urban environment under the frequent/intense NPF. Global PNSDs were discussed more in depth in terms of N_{nuc} (10–25 nm), N_{acc} (100–500 nm), and N_{tot} (10–500 nm). N_{nuc} ratio ($N_{nuc}/(N_{nuc}+N_{acc})$) became generally high in the sites close to anthropogenic sources (60–70% in urban sites), showing significant site-to-site variations. Correlation between N_{tot} and N_{nuc} became higher in urban regions, suggesting N_{tot} are largely dominated by N_{nuc}.

Decadal trends of particle number concentration and NPF frequency were estimated by MK trend test as well as linear regression. For PNSD, decadal change in N_{nuc} was analyzed because it is directly connected NPF occurrence. Most of the urban regions experienced a decrease of N_{nuc}, except for LEI-M. Especially, ANB, DRN, DRW, and KUM showed statistically significant negative trend was detected. N_{nuc} trend became more complex in rural regions according to the transport condition from upwind regions emitting anthropogenic sources, resulting in significant positive trend in BIR and OPE.

Although the magnitude and direction of NPF frequency trend was

similar to those of N_{nuc}, it was not the case in several stations. Especially, LEI-M showed statistically significant positive trend in N_{nuc} but opposite for NPF frequency. As a result, all statistically significant trend of NPF frequency was negative regardless of environmental type of stations. Through the global trend analysis of NPF frequency, the connection between regulations of atmospheric precursors and NPF occurrence was comprehensively revealed for the first time using up-to-date most available PNSD observation in the ambient atmosphere.

To imbue a meaning in terms of climate to the analyzed trend of NPF occurrence, the connection between the change of NPF and potential CCN was investigated. Direct validation was conducted using all available CCN measurement in HYY (2013–2020) and VAV (2008–2016) in this study. Correlation between CCN number concentration and CCN-sized aerosols (e.g. N_{50}, N_{80}, N_{100}) was generally high ($r>0.7$) at representative supersaturation range of ambient atmosphere (0.3%–0.5%) both in HYY and VAV. To exclude the impact from direct emission of accumulation-mode particles on CCN-sized aerosols as much as possible, the lowest size limit (N_{50}) was selected for the potential CCN in this study.

N_{50} during NPF events was significantly higher compared to non-NPF events, showing 76%, 72%, and 170% increase in urban, rural, and remote sites, respectively. Although N_{50} during NPF events in remote sites showed the sharpest increase under the lowest N_{50} during non-NPF

(~400 cm^{-3}), N_{50} increase in urban of relatively high N_{50} during non-NPF (~2500 cm^{-3}) was larger than that in rural sites under generally high GR of aerosol population.

Although the occurrence of NPF might not be directly related to N_{50}, all of the statistically significant trend was negative in both of NPF frequency and N_{50} trend regardless of the observation environments. Considering the significant impact of NPF occurrence on CCN budget estimated in this study, global decadal decrease of potential CCN closely connected with declined NPF frequency can meaningfully modulate precipitation or radiative effect of clouds via influencing on the aerosol indirect effect, resulting in the decreased cloud albedo or increased precipitation associated with larger cloud droplets.

References

Aas W, Eckhardt S, Fiebig M, Solberg S, Yttri K E. Monitoring of long-range transported air pollutants in Norway: Annual Report 2019. NILU report 2020.

Aas W, Mortier A, Bowersox V, Cherian R, Faluvegi G, Fagerli H, et al. Global and regional trends of atmospheric sulfur. Scientific reports 2019; 9: 1-11.

Altstädter B, Platis A, Jähn M, Baars H, Lückerath J, Held A, et al. Airborne observations of newly formed boundary layer aerosol particles under cloudy conditions. Atmospheric Chemistry and Physics 2018; 18: 8249-8264.

Asmi E, Kivekäs N, Kerminen V-M, Komppula M, Hyvärinen A-P, Hatakka J, et al. Secondary new particle formation in Northern Finland Pallas site between the years 2000 and 2010. Atmospheric Chemistry and Physics 2011; 11: 12959-12972.

Atzler F, Wiedensohler A, Roß T, Weinhold K, Dobberkau M. Roller dynamometer particle immission* measurement. Automotive and Engine Technology 2022: 1-12.

Bei N, Zhao L, Wu J, Li X, Feng T, Li G. Impacts of sea-land and mountain-valley circulations on the air pollution in Beijing-Tianjin-Hebei (BTH): A case study. Environmental pollution 2018; 234: 429-438.

Bianchi, F., Tröstl, J., Junninen, H., Frege, C., Henne, S., Hoyle, C. R., et al. New particle formation in the free troposphere: A question of chemistry and timing. Science 2016; 352(6289): 1109-1112.

Birmili W, Rehn J, Vogel A, Boehlke C, Weber K, Rasch F. Micro-scale variability of urban particle number and mass concentrations in Leipzig, Germany. Meteorol. Z 2013; 22: 155-165.

Bousiotis D, Brean J, Pope FD, Dall'Osto M, Querol X, Alastuey A, et al. The

effect of meteorological conditions and atmospheric composition in the occurrence and development of new particle formation (NPF) events in Europe. Atmospheric Chemistry and Physics 2021; 21: 3345-3370.

Boy M, Kulmala M. Nucleation events in the continental boundary layer: Influence of physical and meteorological parameters. Atmospheric Chemistry and Physics 2002; 2: 1-16.

Chang Y, Huang RJ, Ge X, Huang X, Hu J, Duan Y, et al. Puzzling haze events in China during the coronavirus (COVID-19) shutdown. Geophysical Research Letters 2020; 47: e2020GL088533.

Cho C, Schwarz JP, Perring AE, Lamb KD, Kondo Y, Park J-U, et al. Light-absorption enhancement of black carbon in the Asian outflow inferred from airborne SP2 and in-situ measurements during KORUS-AQ. Science of The Total Environment 2021; 773: 145531.

Choi J, Choi Y, Ahn J, Park J, Oh J, Lee G, et al. Observation of secondary organic aerosol and new particle formation at a remote site in baengnyeong Island, Korea. Asian Journal of Atmospheric Environment 2017; 11: 300-312.

Chu B, Dada L, Liu Y, Yao L, Wang Y, Du W, et al. Particle growth with photochemical age from new particle formation to haze in the winter of Beijing, China. Science of the Total Environment 2021; 753: 142207.

Collaud Coen M, Andrews E, Bigi A, Martucci G, Romanens G, Vogt F, et al. Effects of the prewhitening method, the time granularity, and the time segmentation on the Mann–Kendall trend detection and the associated Sen's slope. Atmospheric measurement techniques 2020; 13: 6945-6964.

Crounse JD, McKinney KA, Kwan AJ, Wennberg PO. Measurement of gas-phase hydroperoxides by chemical ionization mass spectrometry. Analytical chemistry 2006; 78: 6726-6732.

Dai L, Wang H, Zhou L, An J, Tang L, Lu C, et al. Regional and local new particle formation events observed in the Yangtze River Delta region, China. Journal of Geophysical Research: Atmospheres 2017; 122: 2389-2402.

Dal Maso M, Kulmala M, Riipinen I, Wagner R, Hussein T, Aalto PP, et al. Formation and growth of fresh atmospheric aerosols: eight years of aerosol size distribution data from SMEAR II, Hyytiälä, Finland. Boreal environment research 2005; 10: 323.

Dall'Osto M, Beddows D, Asmi A, Poulain L, Hao L, Freney E, et al. Novel insights on new particle formation derived from a pan-european observing system. Scientific reports 2018; 8: 1482.

de España CD, Wonaschütz A, Steiner G, Rosati B, Demattio A, Schuh H, et al. Long-term quantitative field study of New Particle Formation (NPF) events as a source of Cloud Condensation Nuclei (CCN) in the urban background of Vienna. Atmospheric Environment 2017; 164: 289-298.

De Persis S, Dollet A, Teyssandier F. Pressure dependence of gas-phase reaction rates. Journal of chemical education 2004; 81: 832.

Debevec C, Sauvage S, Gros V, Sellegri K, Sciare J, Pikridas M, et al. Driving parameters of biogenic volatile organic compounds and consequences on new particle formation observed at an eastern Mediterranean background site. Atmospheric Chemistry and Physics 2018; 18: 14297-14325.

DeCarlo PF, Kimmel JR, Trimborn A, Northway MJ, Jayne JT, Aiken AC, et al. Field-deployable, high-resolution, time-of-flight aerosol mass spectrometer. Analytical chemistry 2006; 78: 8281-8289.

Ding K, Liu J, Ding A, Liu Q, Zhao T, Shi J, et al. Uplifting of carbon monoxide from biomass burning and anthropogenic sources to the free troposphere in East Asia. Atmospheric Chemistry and Physics

2015; 15: 2843-2866.

Fan H, Wang Y, Zhao C, Yang Y, Yang X, Sun Y, et al. The role of primary emission and transboundary transport in the air quality changes during and after the COVID-19 lockdown in China. Geophysical Research Letters 2021; 48: e2020GL091065.

Farah A, Villani P, Rose C, Conil S, Langrene L, Laj P, et al. Characterization of Aerosol Physical and Optical Properties at the Observatoire Pérenne de l'Environnement (OPE) Site. Atmosphere 2020; 11: 172.

Gilardoni S, Vignati E, Cavalli F, Putaud J, Larsen B, Karl M, et al. Better constraints on sources of carbonaceous aerosols using a combined 14 C–macro tracer analysis in a European rural background site. Atmospheric Chemistry and Physics 2011; 11: 5685-5700.

Größ J, Hamed A, Sonntag A, Spindler G, Manninen HE, Nieminen T, et al. Atmospheric new particle formation at the research station Melpitz, Germany: connection with gaseous precursors and meteorological parameters. Atmospheric Chemistry and Physics 2018; 18: 1835-1861.

Hallar A, Petersen R, McCubbin IB, Lowenthal D, Lee S, Andrews E, et al. Climatology of new particle formation and corresponding precursors at Storm Peak Laboratory. 2016.

Hallar AG, Lowenthal DH, Chirokova G, Borys RD, Wiedinmyer C. Persistent daily new particle formation at a mountain-top location. Atmospheric Environment 2011; 45: 4111-4115.

Hamed A, Joutsensaari J, Mikkonen S, Sogacheva L, Dal Maso M, Kulmala M, et al. Nucleation and growth of new particles in Po Valley, Italy. Atmospheric Chemistry and Physics 2007; 7: 355-376.

Hammer E, Bukowiecki N, Gysel M, Jurányi Z, Hoyle CR, Vogt R, et al. Investigation of the effective peak supersaturation for liquid-phase clouds at the high-alpine site Jungfraujoch, Switzerland (3580 m asl).

Atmospheric Chemistry and Physics 2014; 14: 1123-1139.

He G, Pan Y, Tanaka T. The short-term impacts of COVID-19 lockdown on urban air pollution in China. Nature sustainability 2020; 3: 1005-1011.

Heintzenberg J, Senf F, Birmili W, Wiedensohler A. Aerosol connections between three distant continental stations. Atmospheric Environment 2018; 190: 349-358.

Hoyle CR, Webster CS, Rieder HE, Nenes A, Hammer E, Herrmann E, et al. Chemical and physical influences on aerosol activation in liquid clouds: a study based on observations from the Jungfraujoch, Switzerland. Atmospheric Chemistry and Physics 2016; 16: 4043-4061.

Huey LG, Tanner D, Slusher D, Dibb JE, Arimoto R, Chen G, et al. CIMS measurements of HNO3 and SO2 at the South Pole during ISCAT 2000. Atmospheric Environment 2004; 38: 5411-5421.

Hussein T, Mölgaard B, Hannuniemi H, Martikainen J, Järvi L, Wegner T, et al. Fingerprints of Urban Particle Number Size Distribution in Helsinki–Finland: Local versus Regional Characteristics. Boreal environment research 2014.

Jeong C-H, Evans GJ. Inter-comparison of a fast mobility particle sizer and a scanning mobility particle sizer incorporating an ultrafine water-based condensation particle counter. Aerosol Science and Technology 2009; 43: 364-373.

Ji Y, Qin X, Wang B, Xu J, Shen J, Chen J, et al. Counteractive effects of regional transport and emission control on the formation of fine particles: a case study during the Hangzhou G20 summit. Atmospheric Chemistry and Physics 2018; 18: 13581-13600.

Jordan CE, Crawford JH, Beyersdorf AJ, Eck TF, Halliday HS, Nault BA, et al. Investigation of factors controlling PM2. 5 variability across the

South Korean Peninsula during KORUS-AQ. Elementa: Science of the Anthropocene 2020; 8.

Ju MJ, Oh J, Choi Y-H. Changes in air pollution levels after COVID-19 outbreak in Korea. Science of the Total Environment 2021; 750: 141521.

Jung CH, Yoon YJ, Kang HJ, Gim Y, Lee BY, Ström J, et al. The seasonal characteristics of cloud condensation nuclei (CCN) in the arctic lower troposphere. Tellus B: Chemical and Physical Meteorology 2018; 70: 1-13.

Jurányi Z, Gysel M, Weingartner E, Bukowiecki N, Kammermann L, Baltensperger U. A 17 month climatology of the cloud condensation nuclei number concentration at the high alpine site Jungfraujoch. Journal of Geophysical Research: Atmospheres 2011; 116.

Kalkavouras P, Bougiatioti A, Grivas G, Stavroulas I, Kalivitis N, Liakakou E, et al. On the regional aspects of new particle formation in the Eastern Mediterranean: A comparative study between a background and an urban site based on long term observations. Atmospheric Research 2020; 239: 104911.

Kerminen V-M, Chen X, Vakkari V, Petäjä T, Kulmala M, Bianchi F. Atmospheric new particle formation and growth: review of field observations. Environmental Research Letters 2018; 13: 103003.

Kerminen V-M, Paramonov M, Anttila T, Riipinen I, Fountoukis C, Korhonen H, et al. Cloud condensation nuclei production associated with atmospheric nucleation: a synthesis based on existing literature and new results. Atmospheric Chemistry and Physics 2012; 12: 12037-12059.

Khoder MI. Atmospheric conversion of sulfur dioxide to particulate sulfate and nitrogen dioxide to particulate nitrate and gaseous nitric acid in an urban area. Chemosphere 2002; 49: 675-684.

Kim H, Zhang Q, Heo J. Influence of intense secondary aerosol formation and long-range transport on aerosol chemistry and properties in the Seoul Metropolitan Area during spring time: results from KORUS-AQ. Atmospheric Chemistry and Physics 2018; 18: 7149-7168.

Kim K-Y, North GR, Huang J. EOFs of one-dimensional cyclostationary time series: Computations, examples, and stochastic modeling. Journal of Atmospheric Sciences 1996; 53: 1007-1017.

Kim S-W, Heo J, Park J-U. Relationship between submicron particle formation and air mass history observed in the Asian continental outflow at Gosan, Korea, during 2008–2018. Air Quality, Atmosphere & Health 2021; 14: 291-300.

Kim Y, Kim S-W, Yoon S-C. Observation of new particle formation and growth under cloudy conditions at Gosan Climate Observatory, Korea. Meteorology and Atmospheric Physics 2014; 126: 81-90.

Kim Y, Kim S-W, Yoon S-C, Park J-S, Lim J-H, Hong J, et al. Characteristics of formation and growth of atmospheric nanoparticles observed at four regional background sites in Korea. Atmospheric Research 2016; 168: 80-91.

Kim Y, Yoon S-C, Kim S-W, Kim K-Y, Lim H-C, Ryu J. Observation of new particle formation and growth events in Asian continental outflow. Atmospheric environment 2013; 64: 160-168.

Kristensson A, Dal Maso M, Swietlicki E, Hussein T, Zhou J, Kerminen V-M, et al. Characterization of new particle formation events at a background site in Southern Sweden: relation to air mass history. Tellus B: Chemical and Physical Meteorology 2008; 60: 330-344.

Kulmala M, Junninen H, Dada L, Salma I, Weidinger T, Thén W, et al. Quiet New Particle Formation in the Atmosphere. Frontiers in Environmental Science 2022.

Kulmala M, Maso MD, Mäkelä J, Pirjola L, Väkevä M, Aalto P, et al. On the

formation, growth and composition of nucleation mode particles. Tellus B 2001; 53: 479-490.

Kulmala M, Petäjä T, Ehn M, Thornton J, Sipilä M, Worsnop D, et al. Chemistry of atmospheric nucleation: on the recent advances on precursor characterization and atmospheric cluster composition in connection with atmospheric new particle formation. Annual review of physical chemistry 2014; 65: 21-37.

Kulmala M, Vehkamäki H, Petäjä T, Dal Maso M, Lauri A, Kerminen V-M, et al. Formation and growth rates of ultrafine atmospheric particles: a review of observations. Journal of Aerosol Science 2004; 35: 143-176.

Kwak K-H, Han B-S, Park K, Moon S, Jin H-G, Park S-B, et al. Inter-and intra-city comparisons of PM 2.5 concentration changes under COVID-19 social distancing in seven major cities of South Korea. Air Quality, Atmosphere & Health 2021; 14: 1155-1168.

Laj P, Bigi A, Rose C, Andrews E, Lund Myhre C, Collaud Coen M, et al. A global analysis of climate-relevant aerosol properties retrieved from the network of Global Atmosphere Watch (GAW) near-surface observatories. Atmospheric Measurement Techniques 2020; 13: 4353-4392.

Lee Y, Park J, Kim P, Ghim YS. New particle formation and diurnal variations in number concentrations at a rural site downwind of Seoul, Korea. Atmospheric Pollution Research 2021; 12: 214-223.

Lehner M, Rotach MW, Obleitner F. A method to identify synoptically undisturbed, clear-sky conditions for valley-wind analysis. Boundary-Layer Meteorology 2019; 173: 435-450.

Lehtinen K, Kulmala M. A model for particle formation and growth in the atmosphere with molecular resolution in size. Atmospheric Chemistry and Physics 2003; 3: 251-257.

Leinonen V, Kokkola H, Yli-Juuti T, Mielonen T, Kühn T, Nieminen T, et al.

Comparison of particle number size distribution trends in ground measurements and climate models. Atmospheric Chemistry and Physics 2022; 22: 12873-12905.

Li X, Chee S, Hao J, Abbatt JP, Jiang J, Smith JN. Relative humidity effect on the formation of highly oxidized molecules and new particles during monoterpene oxidation. Atmospheric Chemistry and Physics 2019; 19: 1555-1570.

Liu C, Zhang F, Miao L, Lei Y, Yang Q. Future haze events in Beijing, China: When climate warms by 1.5 and 2.0° C. International Journal of Climatology 2019; 40: 3689-3700.

Liu P, Ye C, Xue C, Zhang C, Mu Y, Sun X. Formation mechanisms of atmospheric nitrate and sulfate during the winter haze pollution periods in Beijing: gas-phase, heterogeneous and aqueous-phase chemistry. Atmospheric Chemistry and Physics 2020; 20: 4153-4165.

Lv G, Sui X, Chen J, Jayaratne R, Mellouki A. Investigation of new particle formation at the summit of Mt. Tai, China. Atmospheric Chemistry and Physics 2018; 18: 2243-2258.

Marinescu PJ, Levin EJ, Collins D, Kreidenweis SM, van den Heever SC. Quantifying aerosol size distributions and their temporal variability in the Southern Great Plains, USA. Atmospheric Chemistry and Physics 2019; 19: 11985-12006.

Matsui H, Koike M, Takegawa N, Kondo Y, Takami A, Takamura T, et al. Spatial and temporal variations of new particle formation in East Asia using an NPF-explicit WRF-chem model: North-south contrast in new particle formation frequency. Journal of Geophysical Research: Atmospheres 2013; 118: 11,647-11,663.

Merikanto J, Spracklen D, Mann G, Pickering S, Carslaw K. Impact of nucleation on global CCN. Atmospheric Chemistry and Physics 2009; 9: 8601-8616.

Miao Y, Liu S, Zheng Y, Wang S, Chen B, Zheng H, et al. Numerical study of the effects of local atmospheric circulations on a pollution event over Beijing–Tianjin–Hebei, China. Journal of Environmental Sciences 2015; 30: 9-20.

Mielonen T, Aaltonen V, Lihavainen H, Hyvärinen A-P, Arola A, Komppula M, et al. Biomass burning aerosols observed in northern Finland during the 2010 wildfires in Russia. Atmosphere 2013; 4: 17-34.

Molnár A, Bécsi Z, Imre K, Gácser V, Ferenczi Z. Characterization of background aerosol properties during a wintertime smog episode. Aerosol and Air Quality Research 2016; 16: 1793-1804.

Motos G, Schmale J, Corbin JC, Modini RL, Karlen N, Bertò M, et al. Cloud droplet activation properties and scavenged fraction of black carbon in liquid-phase clouds at the high-alpine research station Jungfraujoch (3580 m asl). Atmospheric Chemistry and Physics 2019; 19: 3833-3855.

National Institute of Environmental Research (NIER), National Aeronautics and Space Administration (NASA), Rapid Science Synthesis Report. 2017. https://espo.nasa.gov/sites/default/files/documents/KORUS-AQ-RSSR.pdf (last access: 17 July 2023)

Nieminen T, Kerminen V-M, Petäjä T, Aalto PP, Arshinov M, Asmi E, et al. Global analysis of continental boundary layer new particle formation based on long-term measurements. Atmospheric Chemistry and Physics 2018; 18: 14737-14756.

Park D-H, Kim JE, Park J-S, Choi J-S, Kim S-W. Impacts of the COVID-19 lockdown in China on new particle formation and particle number size distribution in three regional background sites in Asian continental outflow. Science of The Total Environment 2023; 858: 159904.

Park D-H, Kim S-W, Kim M-H, Yeo H, Park SS, Nishizawa T, et al. Impacts of local versus long-range transported aerosols on PM10 concentrations in Seoul, Korea: An estimate based on 11-year PM10 and lidar observations. Science of the Total Environment 2021a; 750: 141739.

Park J-U, Kim H-J, Choi J, Park J-S, Heo J, Kim S-W. Observation of aerosol size distribution and new particle formation under different air masses arriving at the northwesternmost South Korean island in the Yellow Sea. Atmospheric Research 2021b; 255: 105537.

Park M, Yum SS, Kim JH. Characteristics of submicron aerosol number size distribution and new particle formation events measured in Seoul, Korea, during 2004–2012. Asia-Pacific Journal of Atmospheric Sciences 2015; 51: 1-10.

Park M, Yum SS, Kim N, Anderson BE, Beyersdorf A, Thornhill KL. On the submicron aerosol distributions and CCN activity in and around the Korean Peninsula measured onboard the NASA DC-8 research aircraft during the KORUS-AQ field campaign. Atmospheric research 2020; 243: 105004.

Park, S., Kim, S. W., Park, M. S., & Song, C. K. Measurement of planetary boundary layer winds with scanning doppler lidar. Remote Sensing 2018. 10(8): 1261.

Petäjä T, Mauldin I, RL, Kosciuch E, McGrath J, Nieminen T, Paasonen P, et al. Sulfuric acid and OH concentrations in a boreal forest site. Atmospheric Chemistry and Physics 2009; 9: 7435-7448.

Petäjä T, Tabakova K, Manninen A, Ezhova E, O'Connor E, Moisseev D, et al. Influence of biogenic emissions from boreal forests on aerosol–cloud interactions. Nature Geoscience 2022; 15: 42-47.

Peterson DA, Hyer EJ, Han S-O, Crawford JH, Park RJ, Holz R, et al. Meteorology influencing springtime air quality, pollution transport,

and visibility in Korea. Elementa: Science of the Anthropocene 2019; 7.

Pushpawela B, Jayaratne R, Morawska L. The influence of wind speed on new particle formation events in an urban environment. Atmospheric Research 2019; 215: 37-41.

Qi X, Ding A, Nie W, Chi X, Huang X, Xu Z, et al. Direct measurement of new particle formation based on tethered airship around the top of the planetary boundary layer in eastern China. Atmospheric environment 2019; 209: 92-101.

Quan J, Liu Y, Liu Q, Jia X, Li X, Gao Y, et al. Anthropogenic pollution elevates the peak height of new particle formation from planetary boundary layer to lower free troposphere. Geophysical Research Letters 2017; 44: 7537-7543.

Rose C, Collaud Coen M, Andrews E, Lin Y, Bossert I, Lund Myhre C, et al. Seasonality of the particle number concentration and size distribution: a global analysis retrieved from the network of Global Atmosphere Watch (GAW) near-surface observatories. Atmospheric Chemistry and Physics 2021; 21: 17185-17223.

Rose C, Foucart B, Picard D, Colomb A, Metzger J-M, Tulet P, et al. New particle formation in the volcanic eruption plume of the Piton de la Fournaise: specific features from a long-term dataset. Atmospheric Chemistry and Physics 2019; 19: 13243-13265.

Rose C, Sellegri K, Freney E, Dupuy R, Colomb A, Pichon J-M, et al. Airborne measurements of new particle formation in the free troposphere above the Mediterranean Sea during the HYMEX campaign. Atmospheric Chemistry and Physics 2015; 15: 10203-10218.

Rose C, Sellegri K, Moreno I, Velarde F, Ramonet M, Weinhold K, et al. CCN production by new particle formation in the free troposphere.

Atmospheric Chemistry and Physics 2017; 17: 1529-1541.

Rose C, Sellegri K, Velarde F, Moreno I, Ramonet M, Weinhold K, et al. Frequent nucleation events at the high altitude station of Chacaltaya (5240 m asl), Bolivia. Atmospheric Environment 2015; 102: 18-29.

Saha PK, Robinson ES, Shah RU, Zimmerman N, Apte JS, Robinson AL, et al. Reduced ultrafine particle concentration in urban air: changes in nucleation and anthropogenic emissions. Environmental science & technology 2018; 52: 6798-6806.

Schladitz A, Leníček J, Beneš I, Kováč M, Skorkovský J, Soukup A, et al. Air quality in the German–Czech border region: A focus on harmful fractions of PM and ultrafine particles. Atmospheric Environment 2015; 122: 236-249.

Seinfeld JH, Pandis SN. Atmospheric chemistry and physics: from air pollution to climate change: John Wiley & Sons, 2016.

Shen J, Bigi A, Marinoni A, Lampilahti J, Kontkanen J, Ciarelli G, et al. Emerging Investigator Series: COVID-19 lockdown effects on aerosol particle size distributions in northern Italy. Environmental science: atmospheres 2021a; 1: 214-227.

Shen X, Sun J, Yu F, Wang Y, Zhong J, Zhang Y, et al. Enhancement of nanoparticle formation and growth during the COVID-19 lockdown period in urban Beijing. Atmospheric Chemistry and Physics 2021b; 21: 7039-7052.

Shen X, Sun J, Zhang X, Kiveka N, Zhang Y, Wang T, et al. Particle climatology in Central East China retrieved from measurements in planetary boundary layer and in free troposphere at a 1500-m-High mountaintop site. Aerosol and Air Quality Research 2016; 16: 689-701.

Shi X, Brasseur GP. The response in air quality to the reduction of Chinese economic activities during the COVID-19 outbreak. Geophysical

Research Letters 2020; 47: e2020GL088070.

Shrestha AM, Shrestha UB, Sharma R, Bhattarai S, Tran HNT, Rupakheti M. Lockdown caused by COVID-19 pandemic reduces air pollution in cities worldwide. 2020.

Simpson IJ, Blake DR, Blake NJ, Meinardi S, Barletta B, Hughes SC, et al. Characterization, sources and reactivity of volatile organic compounds (VOCs) in Seoul and surrounding regions during KORUS-AQ. Elementa: Science of the Anthropocene 2020; 8.

Skrabalova L, Zikova N, Zdimal V. Shrinkage of newly formed particles in an urban environment. Aerosol and Air Quality Research 2015; 15: 1313-1324.

Slusher DL, Huey LG, Tanner DJ, Flocke FM, Roberts JM. A thermal dissociation–chemical ionization mass spectrometry (TD-CIMS) technique for the simultaneous measurement of peroxyacyl nitrates and dinitrogen pentoxide. Journal of Geophysical Research: Atmospheres 2004; 109.

Spracklen DV, Carslaw KS, Kulmala M, Kerminen VM, Sihto SL, Riipinen I, et al. Contribution of particle formation to global cloud condensation nuclei concentrations. Geophysical Research Letters 2008; 35.

Sun, J., Birmili, W., Hermann, M., Tuch, T., Weinhold, K., Spindler, G., et al. Variability of black carbon mass concentrations, sub-micrometer particle number concentrations and size distributions: results of the German Ultrafine Aerosol Network ranging from city street to High Alpine locations. Atmospheric Environment 2019 202: 256-268.

Sun W, Shao M, Granier C, Liu Y, Ye C, Zheng J. Long-term trends of Anthropogenic SO2, NOx, CO, and NMVOCs emissions in China. Earth's Future 2018; 6: 1112-1133.

Takegawa N, Seto T, Moteki N, Koike M, Oshima N, Adachi K, et al. Enhanced new particle formation above the marine boundary layer

over the Yellow Sea: Potential impacts on cloud condensation nuclei. Journal of Geophysical Research: Atmospheres 2020; 125: e2019JD031448.

Tang L, Shang D, Fang X, Wu Z, Qiu Y, Chen S, et al. More significant impacts from new particle formation on haze formation during COVID-19 lockdown. Geophysical Research Letters 2021; 48: e2020GL091591.

Tian J, Wang Q, Zhang Y, Yan M, Liu H, Zhang N, et al. Impacts of primary emissions and secondary aerosol formation on air pollution in an urban area of China during the COVID-19 lockdown. Environment International 2021; 150: 106426.

Tian M, Liu Y, Yang F, Zhang L, Peng C, Chen Y, et al. Increasing importance of nitrate formation for heavy aerosol pollution in two megacities in Sichuan Basin, southwest China. Environmental Pollution 2019; 250: 898-905.

Tsona NT, Li J, Du L. From O2−-initiated SO2 oxidation to sulfate formation in the gas phase. The Journal of Physical Chemistry A 2018; 122: 5781-5788.

Tunved P, Ström J. On the seasonal variation in observed size distributions in northern Europe and their changes with decreasing anthropogenic emissions in Europe: climatology and trend analysis based on 17 years of data from Aspvreten, Sweden. Atmospheric Chemistry and Physics 2019; 19: 14849-14873.

Väänänen R, Krejci R, Manninen HE, Manninen A, Lampilahti J, Buenrostro Mazon S, et al. Vertical and horizontal variation of aerosol number size distribution in the boreal environment. Atmospheric Chemistry and Physics Discussions 2016: 1-43.

Vana M, Komsaare K, Hõrrak U, Mirme S, Nieminen T, Kontkanen J, et al. Characteristics of new-particle formation at three SMEAR stations.

Boreal Environment Research 2016.

Venter ZS, Aunan K, Chowdhury S, Lelieveld J. COVID-19 lockdowns cause global air pollution declines. Proceedings of the National Academy of Sciences 2020; 117: 18984-18990.

Vratolis S, Gini M, Bezantakos S, Stavroulas I, Kalivitis N, Kostenidou E, et al. Particle number size distribution statistics at City-Centre Urban Background, urban background, and remote stations in Greece during summer. Atmospheric environment 2019; 213: 711-726.

Wang D, Zhou B, Fu Q, Zhao Q, Zhang Q, Chen J, et al. Intense secondary aerosol formation due to strong atmospheric photochemical reactions in summer: Observations at a rural site in eastern Yangtze River Delta of China. Science of the Total Environment 2016; 571: 1454-1466.

Wang Z, Birmili W, Hamed A, Wehner B, Spindler G, Pei X, et al. Contributions of volatile and nonvolatile compounds (at 300 C) to condensational growth of atmospheric nanoparticles: an assessment based on 8.5 years of observations at the central Europe background site Melpitz. Journal of Geophysical Research: Atmospheres 2017; 122: 485-497.

Wiedensohler, A., Birmili, W., Nowak, A., Sonntag, A., Weinhold, K., Merkel, et al. Mobility particle size spectrometers: harmonization of technical standards and data structure to facilitate high quality long-term observations of atmospheric particle number size distributions. Atmospheric Measurement Techniques 2012; 5(3): 657-685.

Wu L, Sun J, Zhang X, Zhang Y, Wang Y, Zhong J, et al. Aqueous-phase reactions occurred in the PM2. 5 cumulative explosive growth during the heavy pollution episode (HPE) in 2016 Beijing wintertime. Tellus B: Chemical and Physical Meteorology 2019; 71: 1620079.

Yao L, Garmash O, Bianchi F, Zheng J, Yan C, Kontkanen J, et al.

Atmospheric new particle formation from sulfuric acid and amines in a Chinese megacity. Science 2018; 361: 278-281.

Yu X, Cheng T, Chen J, Liu Y. A comparison of dust properties between China continent and Korea, Japan in East Asia. Atmospheric Environment 2006; 40: 5787-5797.

Yue D, Hu M, Zhang R, Wang Z, Zheng J, Wu Z, et al. The roles of sulfuric acid in new particle formation and growth in the mega-city of Beijing. Atmospheric Chemistry and Physics 2010; 10: 4953-4960.

Zhang H, Zhang L, Yang L, Zhou Q, Zhang X, Xing W, et al. Impact of COVID-19 outbreak on the long-range transport of common air pollutants in KUWAMS. Chemical and Pharmaceutical Bulletin 2021; 69: 237-245.

Zhao S, Yu Y, Yin D, He J. Meteorological dependence of particle number concentrations in an urban area of complex terrain, Northwestern China. Atmospheric Research 2015; 164: 304-317.

Zíková N, Ždímal V. Long-term measurement of aerosol number size distributions at rural background station Košetice. Aerosol and Air Quality Research 2013; 13: 1464-1474.

국문 초록

지역 및 전구적 관점에서의 이차 입자 생성 및 후속 성장 경향 분석

박도현

지구환경과학부

서울대학교 대학원

Korea-Unites States Air Quality (KORUS-AQ) 관측 캠페인 기간 동안에 수행된 항공 관측을 바탕으로 한반도 자유대기의 이차 입자 생성(new particle formation)과 관계된 주요 이차 무기 화학종 및 화학 반응 과정의 특징을 조사하였다. 2016 년 5 월 31 일의 황해상 자유대기 이차 입자 생성 사례에는 이산화황으로부터 황산염으로의 전환 과정이 지대한 기여를 했을 것으로 생각되었다. 일산화탄소에 대한 황산염의 비율은 기온 및 상대습도와 모두 양의 상관관계를 지니고 있었는데, 이를 통해 수용액상뿐만 아니라 기체상 반응 경로 또한 황산염 형성에 영향을 미쳤다는 것을 알 수 있었다. 특히 자유대기 이차 입자 생성은 대륙으로부터 얕은 해상 대기경계층으로의 이산화황 전구물질 수송 하에서 적은 에어로졸 표면적 및 강한 태양복사와 같은 자유대기만의 이차 입자 생성 발생 호조건과 관계되어 있을 수 있다. 추가적으로 3–10 nm 직경 초미립자 수농도의 수직적 분포를 통해 KORUS-AQ 관측 캠페인 기간 중 전체적인 이차 입자 생성의 특성을 살펴보았다. 초미립자 수농도는 1 km 고도 이하에서

최대(7606±12003 cm^{-3})를 보여, 한반도 이차 입자 생성은 자유대기 보다는 대기경계층 내부에서 더 빈번하게 혹은 강하게 발생한다는 점을 확인하였다.

대기 전구물질의 배출 변화가 이차 입자 생성 발생에 미치는 영향은, 전구물질 증기와 기존재하는 큰 입자가 만들어내는 응결/응고 싱크 간의 관계에 의해서 결정되기 때문에 상당히 복잡하게 나타날 수 있다. 따라서 코로나로 인한 봉쇄조치 기간동안 3 개의 지표 배경대기 관측소(백령도, 안면도, 제주 봉성)에서 얻어진 입자 크기 분포 관측자료를 바탕으로 동아시아 지역에서 응결 증기의 시간적 변화가 입자 크기 분포(particle number size distribution)에 미치는 영향을 평가하였다. 핵화모드(< 25 nm) 및 축적모드(> 90 nm) 입자의 수농도는 봉쇄조치 기간동안 백령도에서 각각 약 34%, 29% 감소를 보였다. 그러나 안면도는 국지 배출의 영향 하에서 핵화 및 축적모드 입자의 미미한 감소만이 이루어졌다. 제주 봉성은 봉쇄조치 기간동안 백령도의 입자 크기 분포와 유사한 변화를 보였으나, 상대적으로 높은 고도로 인해 그 감소폭은 상대적으로 적었다(핵화모드 및 축적모드에서 각각 11%, 24% 감소).

객관적인 수치를 이용하여 이차 입자 생성 사례를 비사례로부터 구분하기 위하여 관측된 입자 크기 분포에 Cyclostationary empirical orthogonal function (CSEOF) 기법을 적용하였다. 관측된 입자 크기 분포 자료로부터 추출된 첫 번째 모드의 로딩 벡터가 세 지역에서 모두 소위 바나나 모양이라고 불리는 이차 입자 생성 동안의 전형적인 일변화를 나타내고 있었기 때문에, 그에 해당하는 첫 번째 모드의 주성분 진폭이 이차 입자 생성 사례 분류에 이용되었다. 봉쇄조치 기간동안 이차

입자 생성 발생의 기상학적 호조건이 만들어졌음에도 이차 입자 생성 빈도는 백령도, 안면도, 제주 봉성에서 각각 7%, 1%, 7% 감소하였다. 이차 입자 생성 발생 시간대(오전 8–12 시) 동안에 산출된 황산 추적자 분석 결과, 안면도 및 제주 봉성에서는 봉쇄조치 기간동안 감소한 황산 추적자가 이차 입자 생성 발생의 결정적인 요인으로 작용하였으나, 백령도의 이차 입자 생성 발생은 황산 추적자 변동과 관계가 없었다. 근처 국지 배출원의 부재와 낮은 고도가 만들어내는 시너지 효과를 고려해볼 때, 백령도는 다른 두 지역에 비해 높은 응결 싱크에 대한 황산 추적자 비율(~13.684±13.715 ppb W m^{-2} s)로부터 예상되는 황산 추적자의 포화 하에서 다른 지역에 비해 대륙 기원의 유기 화학종의 감소에 더욱 직접적인 영향을 받았을 것으로 사료된다.

In-Situ AeRosol GAW Network (SARGAN)에 참여중인 관측소들에서 측정된 전구 입자 크기 분포 자료 분석을 통해 입자 크기 분포 및 이차 입자 생성 분석의 시공간적 규모 확장을 도모해 보았다. 먼저 이용 가능한 연속 관측 자료가 5 년보다 긴 관측소들만을 선택하여(27 개 관측소; 도시지역 8 개, 시골지역 15 개, 배경대기지역 4 개) 입자 크기 분포와 이차 입자 생성의 환경적 특성을 상세히 분석해보았다. CSEOF 기법을 기반으로 산정된 이차 입자 생성 빈도는 도시 지역에서 약 43%를 보이며 가장 높았다. 인위적 영향이 최소화되는 관측 환경에서 전반적으로 낮은 이차 입자 생성 빈도가 산출되었다. 이는 실제 대기에서 관측 환경별 전구물질 배출의 차이가 기존재하는 큰 입자로부터 만들어지는 응결 혹은 응고 싱크의 차이보다 이차 입자 생성 발생에 있어서 더 중요한 요인일 수 있다는 점을 시사한다. 전구 입자 크기 분포에 대해서는 총 수농도(10–500 nm),

핵화 모드 입자 수농도(10–25 nm), 축적 모드 입자 수농도(100–500 nm)로 나누어 입자 직경에 따라 체계적인 분석을 수행하였다. 핵화 및 축적모드 입자 수농도의 합에 대한 핵화모드 입자 수농도 비율로 정의되는 핵화모드 입자 비율은 가장 높은 총 수농도를 보이는 도시 지역에서 가장 높았으며(60–70%), 이는 에어로졸 총 수농도를 설명하는 데에 있어서 이차 입자 생성의 빈도 혹은 강도의 중요성을 시사한다. 다른 지역에 비해 도시 지역에서는 입자 크기 분포의 단일봉 분포 상 가장 작은 정점 직경(~19 nm)를 보여, 이차 입자 생성이 입자 크기 분포에 미치는 지대한 영향 또한 확인하였다. 이차 입자 생성 발생이 입자 크기 분포에 미치는 영향은 또한 전구적 경향에서도 확인되었다. 모든 통계적으로 유의한 이차 입자 생성 빈도의 경향은 관측 환경과 관계없이 전부 감소 경향이었다. 또한 대부분의 관측소에서 이차 입자 생성 감소 경향은 핵화 모드 수농도의 감소 경향으로 이어졌다. 더욱이 모든 관측 환경에서 십수년간의 이차 입자 생성 빈도의 감소는 또한 50 nm 보다 큰 잠재적 구름응결핵 수농도의 감소 경향과 긴밀하게 연관되어 있었다. 이는 통계적으로 유의한 전구 이차 입자 생성 빈도 감소 경향이 구름응결핵 크기 에어로졸을 잠재적 구름응결핵으로 취급하는 접근 하에서 구름 응결핵의 전구적인 감소와 연관 되어있을 수 있다는 것을 시사한다.

주요어: 이차 입자 생성, 입자 크기 분포, 구름응결핵, CSEOF 기법, 이차 무기 에어로졸, 코로나 바이러스 봉쇄조치

학 번: 2015-22658